Journal of African Earth Sciences 154 (2019) 136–163

Contents lists available at ScienceDirect

Journal of African Earth Sciences

journal homepage: www.elsevier.com/locate/jafrearsci

Crustal anatexis in the Aouli-Mibladen granitic complex: A window into the middle crust below the Moroccan Eastern Variscan Meseta

Mustapha Elabouyi[a], Mohamed Dahire[a], Youssef Driouch[a,*], Stéphanie Duchêne[b], Leo M. Kriegsman[c,d], Ahmed Ntarmouchant[a], Zia Steven Kahou[b], Jean Luc Severac[b], Mohammed Belkasmi[a], Pierre Debat[b]

[a] Département de Géologie, Laboratoire LGRN, Université Mohamed Ben Abdellah, Faculté des Sciences Dhar El Mahraz, B.P. 1796, Fès-Atlas, Fès, Morocco
[b] Laboratoire GET, Université Paul Sabatier, Toulouse, CNRS, IRD, OMP, 14 Avenue Edouard Belin, 31400, Toulouse, France
[c] Naturalis Biodiversity Center, Leiden, Netherlands
[d] Utrecht University, Faculty of Geosciences, Department of Earth Sciences, Netherlands

ARTICLE INFO

Keywords:
Variscan
Metapelites
Partial melting
Peraluminous granites
Xenoliths
Garnet
Pseudosections

ABSTRACT

The Moroccan Variscan belt comprises numerous granitoid bodies, which have been isotopically studied, but still lack a detailed petrogenetic model. The Variscan Aouli-Mibladen granitic complex in the Moroccan Eastern Meseta provides an excellent opportunity for studying the petrogenesis and the relationship with adjacent Cambro-Ordovician metasediments. This region exposes mainly M-to I-type metaluminous mafic to granitic bodies as well as migmatites and peraluminous S-type anatectic granites. An exceptional xenoliths and garnets cumulate deposit covers an area of ~2 km^2 located NE of the complex. The S-type suite includes cordierite bearing microgranite dykes and two small two-mica leucogranitic stocks, crosscutting the eastern metamorphic aureole of the complex.

Petrological analysis shows that biotite dehydration melting reactions produced anatectic melt and peritectic cordierite and garnet. Garnet shows complex zoning profiles, with typical prograde growth zoning in the core, and resorption and reprecipitation rims. Peritectic cordierite (X_{Fe} = 0.37) is associated with restitic biotite (X_{Fe} = 0.65), whereas abundant cotectic cordierite (X_{Fe} = 0.65) belongs to the granites paragenesis (Bt + Kfs + Pl + Crd + Qtz). Garnet crystals are also frequently mantled by a retrograde cordierite type.

Thermodynamic modelling shows that biotite dehydration melting took place under granulitic facies conditions (830–870 °C and 6 kbar), producing a significant amount of peraluminous melts. Their ascent and emplacement led to the S-type suite of the Aouli-Mibladen complex, including the local xenolith-cumulate deposit. We envisage a petrogenetic model during the Variscan orogeny, in which mantle derived mafic magmas stagnated in large reservoirs at 18–20 km depth, causing isobaric heating and partial melting of the surrounding metapelitic protolith. Differentiated M-I-type and S-type magmas were emplaced at higher levels concomitantly, with limited mixing and mingling during their final crystallization, at a depth of 9–10 km leading to contact metamorphism (600 °C, 3 kbar). These findings open a window into the hitherto unknown Moroccan Variscan mid-crust and permit to discuss the nature and age of the underlying basement terranes.

1. Introduction

The structural evolution of the Morrocan Variscan belt is marked, between 340 and 270 Ma, by the emplacement of numerous granitoid plutons, exposed in Moroccan Mesetas (Fig. 1) north of the South High Atlas fault (Tichka, Jebilets, Rehamna, Zaer, Oulmes and Ment massifs). Their emplacement took place at different crustal levels producing contact metamorphism superimposed on an anchizonal to maximum epizonal regional metamorphism. The Tichka massif (Fig. 1) shows the highest-grade emplacement conditions (680 °C, 3 kbar) with the development of biotite, garnet, andalusite and sillimanite zones in the intruded pelitic rocks (Termier and Termier, 1971; Gasquet, 1991). Other massifs, except for the Aouli-Mibladen massif (Fig. 1) studied in this work, record pressures around 2.4–2.5 kbar at temperatures varying from 550 to 650 °C

* Corresponding author.
E-mail addresses: elabouyi.grm09@gmail.com (M. Elabouyi), dahirem@yahoo.fr (M. Dahire), ydriouch@gmail.com, youssef.driouch@usmba.ac.ma (Y. Driouch), stephanie.duchene@get.omp.eu (S. Duchêne), Leo.Kriegsman@naturalis.nl (L.M. Kriegsman), ahmedntarm@gmail.com (A. Ntarmouchant), Zia.Steven.KAHOU@get.omp.eu (Z.S. Kahou), jeanluc.severac1@libertysurf.fr (J.L. Severac), mbelkasmi@hotmail.com (M. Belkasmi), mireille.debat@wanadoo.fr (P. Debat).

https://doi.org/10.1016/j.jafrearsci.2019.03.006
Received 4 October 2018; Received in revised form 31 January 2019; Accepted 11 March 2019
Available online 26 March 2019
1464-343X/

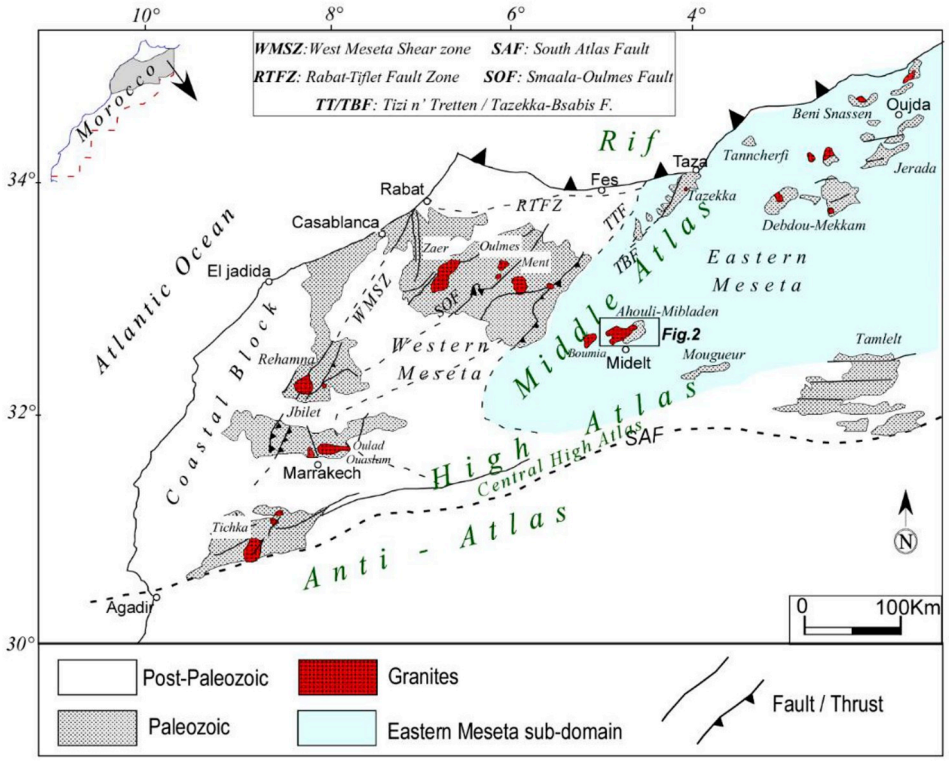

Fig. 1. Simplified geological map of Northern Morocco showing the Paleozoic (meta) sediments and Variscan granitoids (modified from Michard et al., 2010).

Table 1
Major elements whole rocks compositions of Aouli-Mibladen S-type rock suite.

R. type	HLA Migmatite		HLA Anatectic granite		CEE granite	Microgranitic dyke	Two-mica granite		
Sample	MIGT1	MIGT2	GCrd1	GCrd2	MCEE	FGB2	GMP	218P	7C
SiO_2	62.28	56.79	76.28	73.52	77.85	74.50	72.85	72.10	74.95
TiO_2	0.96	1.06	0.06	0.09	0.18	0.07	0.20	0.17	0.15
Al_2O_3	19.82	22.41	13.17	14.49	12.76	14.26	14.63	15.11	14.45
FeOT	6.74	6.27	0.22	0.75	1.19	0.57	1.56	1.40	1.00
MnO	0.14	0.12	0.01	0.03	0.03	0.03	0.05	0.05	0.03
MgO	1.69	1.53	0.06	0.14	0.47	0.06	0.46	0.35	0.30
CaO	0.25	0.50	0.82	0.90	2.19	0.44	0.94	0.88	0.73
Na_2O	1.39	2.19	3.31	3.28	2.88	3.56	3.38	3.35	4.52
K_2O	3.83	5.14	4.40	5.26	0.97	4.77	4.19	4.57	2.09
P_2O_5	0.11	0.17	0.19	0.22	0.09	0.37	0.23	0.21	–
LOI	1.85	2.04	0.72	0.98	0.84	1.03	1.10	1.18	1.20
Total	99.05	98.21	99.23	99.65	99.45	99.67	99.59	99.37	99.42

(Mahmood, 1980; Hoepffner, 1982; Boushaba, 1984; Chemsseddoha, 1986; Dahmani and Sawyer, 2001). Their geodynamic context is controlled by transcurrent tectonics (Diot et al., 1989; El Hadi et al., 2003).

According to the classification of Chappell and White (1974, 2001), White and Chappell (1977, 1983) and Barbarin (1990), three types of magmatic associations have been defined in Moroccan Variscan granitoids: i) calc-alkaline series of mantellic (M-type) or meta-igneous origin (I-type); ii) peraluminous leucogranites of crustal origin (S-type) and; iii) sub-alkaline monzonitic series interpreted as the result of mixed M-, I– and S-type magmas (Rosé, 1987; Mrini et al., 1992; Gasquet et al., 1996; Essaifi et al., 2014). Some sub-types of granites have also been defined in the different massifs based on their petrographic or geochemical characters. The granitoids of the calc-alkaline series of M-I-type origin are largely predominant.

In the Moroccan Variscan belt, the regional metamorphism PT conditions nowhere exceed the greenschist facies conditions, except along the NE-SW trending Western Meseta Shear Zone (Fig. 1, Michard et al., 2010 and Wernert et al., 2016). In the absence of metamorphic and anatectic domes and complexes, direct data on the middle and lower crust are missing. Only few studies on metasedimentary xenoliths have brought indirect information on their metamorphic conditions and age patterns. The more important ones are: i) Moukadiri and Bouloton (1998) and Moukadiri (1999) on the metasedimentary xenoliths included in the quaternary basalts of the Middle Atlas chain (Fig. 1), equilibrated at granulite facies conditions (9–10 kbar and 900 °C) during the Variscan orogeny (Hoeflaken, 2012); ii) Haïmeur et al. (2003) on aluminous enclaves of the Zaër granite pluton (Fig. 1), equilibrated at low-pressure amphibolite facies conditions (750 °C and 3.5 kbar) and; iii) Bouloton (1992), Bouloton et al. (1991) and Gasquet and Bouloton (1995) on the hyperaluminous enclaves of the granites of Oulad Ouaslam (Jebilet massif, Fig. 1) which record original metamorphic conditions of 750 °C and 3 kbar before their transport by granitic magmas en route to their final emplacement.

However, M- and I-type calc-alkaline granites of at least two Variscan granite complexes (Tichka massif in Central High Atlas and Aouli-Mibladen SW eastern meseta) (Fig. 1), are associated with anatexites including migmatites and Crd-Grt bearing anatectic granites

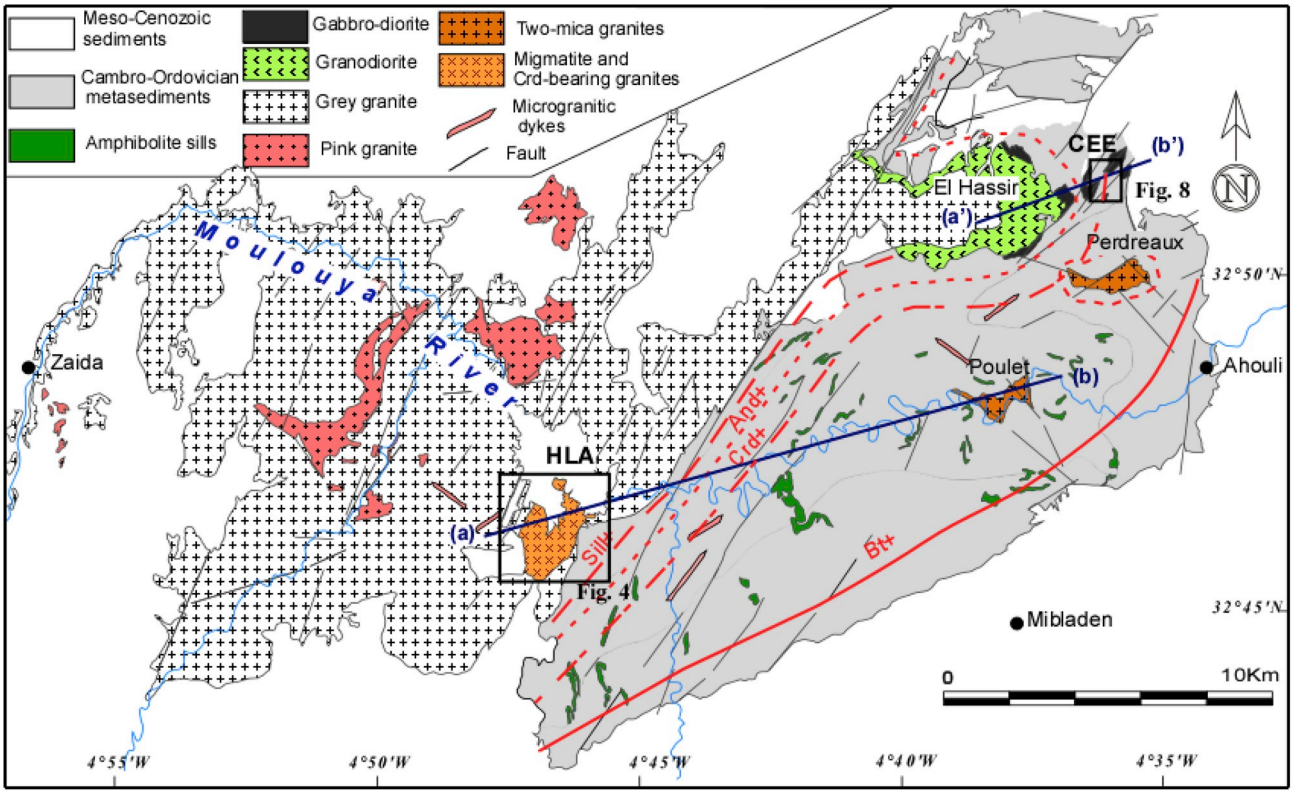

Fig. 2. Geological map of the Aouli Mibladen granitoid complex (modified from Emberger, 1965).

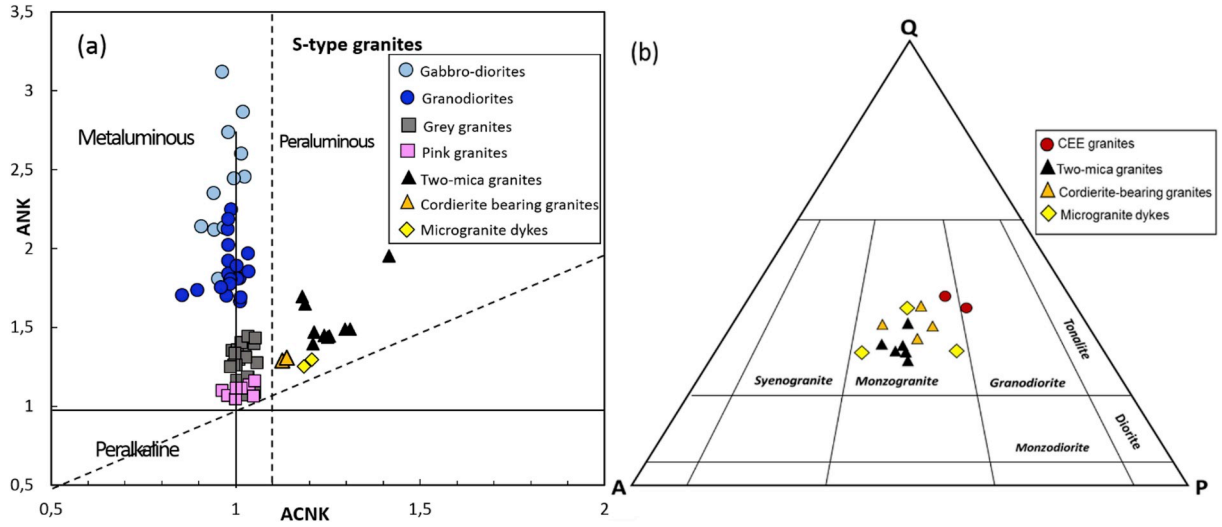

Fig. 3. (a): Diagram showing ANK (Al2O3/[Na2O + K2O], molar proportions) vs. ASI (Al2O3/[CaO + K2O + Na2O], molar proportions) (Maniar and Piccoli, 1989) for granitoid rocks of the Aouli-Mibladen complex. The dashed line (ASI = 1.1) divides the I-type (< 1.1) and S-type (> 1.1) fields of Chappell (1999). (b): Streckeisen diagram of the S-type granitic rocks of Aouli-Mibladen complex.

resulting from crustal melting. This association of M-I-type granites and S-type granites is uncommon in the Moroccan Variscan belt. The definition of partial melting conditions is of great importance in the reconstitution and definition of the thermal state at the structural level where melting took place. It is also crucial in the understanding of the petrogenesis of the S-type granites and their genetic and structural relationships with M-I-type granites (see, for example, Barbey et al., 1990; Montel et al., 1992; Nyman et al., 1995; Vanderhaeghe et al., 1999; Brown and Solar, 1999; Mengel et al., 2001; Milord et al., 2001; and Villaros et al., 2009a,b).

The present work focuses on a petrogenetic study of anatexites and associated rocks in the Aouli-Mibladen granitic complex (High Moulouya, Eastern Moroccan Meseta, Fig. 1). The main objectives are: i) to provide field, petrographic and chemical data on the various anatectic bodies and their components and to investigate the conditions of the partial melting, using classical and modelling methods; and ii) to propose a petrogenetic model for the evolution of this section of the Moroccan Variscan belt.

2. Methods

Whole rocks analysis shown in Table 1 were performed at the SARM, Nancy (France) using ICP-OES method presented in Carignan et al. (2001). Mineral compositions were determined at the Geosciences-Environment-Toulouse (GET) laboratory of the Paul Sabatier

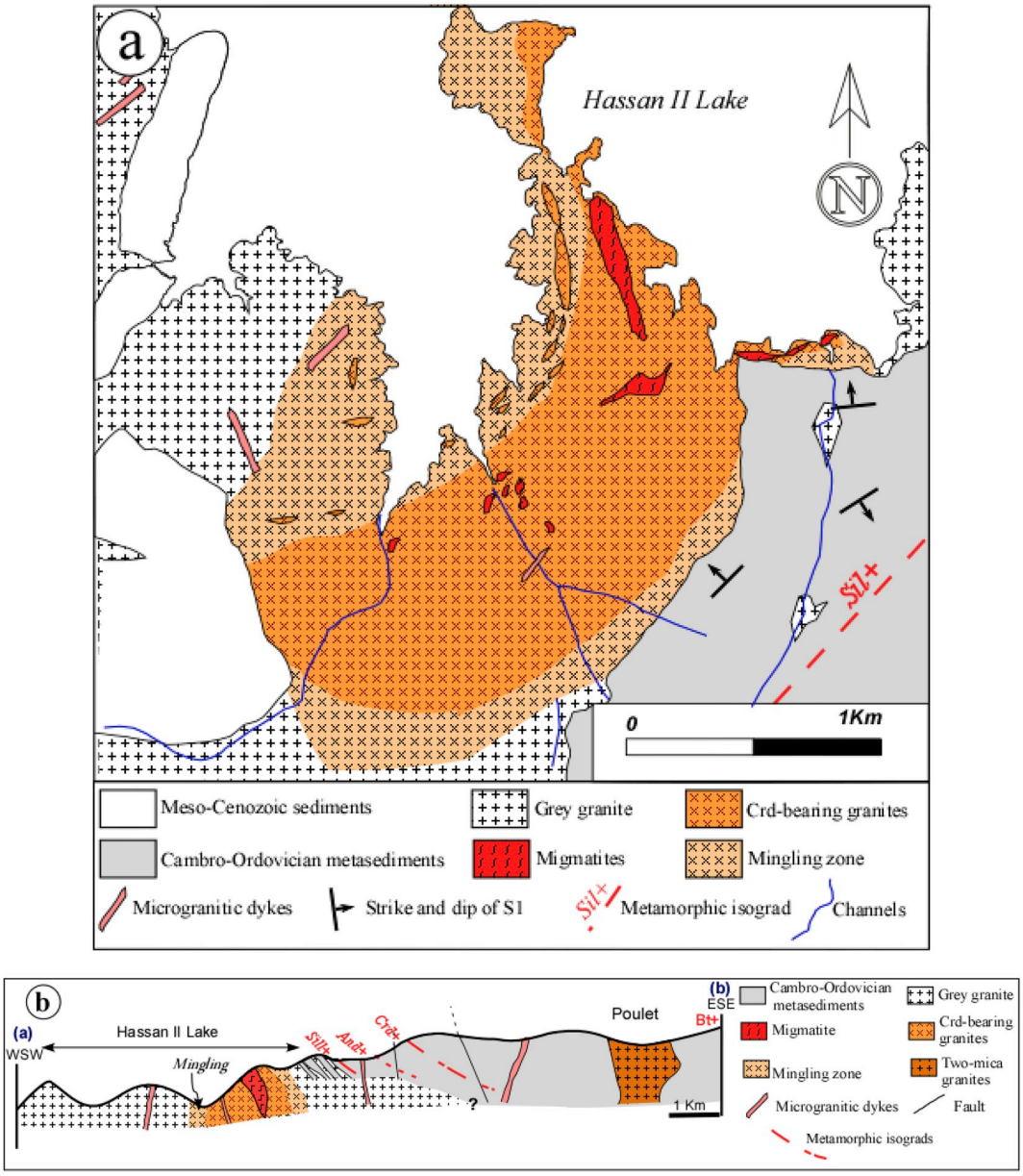

Fig. 4. (a) Geological map of Hassan II Lake Area (HLA); (b) Schematic geological section along the profile a–b on Fig. 2 showing structural relationships between HLA granites and their surroundings.

University in Toulouse (France) with a CAMECA SX50 electron microprobe with SAMx automation, using an accelerating voltage of 15 kV, a beam current of 10 nA, and a beam diameter of 1–5 μm for all elements. Both natural and synthetic standards were used for calibration. Garnets have been analysed by automatic transects and element mapping. We use element transects to construct zoning profiles and compare them to the element maps, giving more precise indications of garnet composition and zoning features.

The pressure–temperature (P–T) estimates are made via Perple_X computer program (Connolly, 2005, 2009; Connolly and Petrini, 2002) using the thermodynamic database of Holland and Powell (1998, with updates). Compositions of minerals as a function of temperature and pressure were calculated from the werami.exe routine of the Perple_X software set to allow their comparison with real compositions of mineral phases in the peraluminous suite of the Aouli-Mibladen complex.

3. Geological setting

The Variscan Aouli-Mibladen complex is located in the southwestern part of the Paleozoic Eastern Moroccan Meseta at the junction of the Central High and Middle Atlas (Fig. 1). The hosting rocks of the Ahouli-Mibladen granitic complex consist of undated schists and amphibolites ascribed to the Lower Paleozoic ("Cambrian-Ordovician"; Hoepffner et al., 2006.). The synmetamorphic folding of the schists has been dated at 366 ± 7 Ma (Rb/Sr whole rock; Clauer et al., 1980). A large contact metamorphic aureole grading from the biotite zone in its external parts to the sillimanite zone at the granite contacts (Fig. 2) is well exposed. Peak pressure-temperature conditions have been estimated at 2.5–3 kbar and 550–600 °C in the sillimanite zone (Filali et al., 1999), corresponding to a final emplacement of the complex at a depth of about 9–10 km. The granites and hosting rocks are unconformably overlain by their unconformable Triassic to Quaternary cover (Fig. 2; Carte géologique du Maroc Echelle 1/50 000: Mibladen. Notes Mém. Serv. Carte géol. Maroc N° 576). The complex comprises three magmatic suites defined by their petrographical and geochemical characters and isotopic data (Emberger, 1965; El Mouraouah, 1993; Oukemini and Bourne, 1994; Oukemini, 1993; Filali, 1996; Filali et al., 1999; Dahire et al., 2002 and Dahire, 2004): a basic to intermediate suite, a metaluminous granitic suite and a

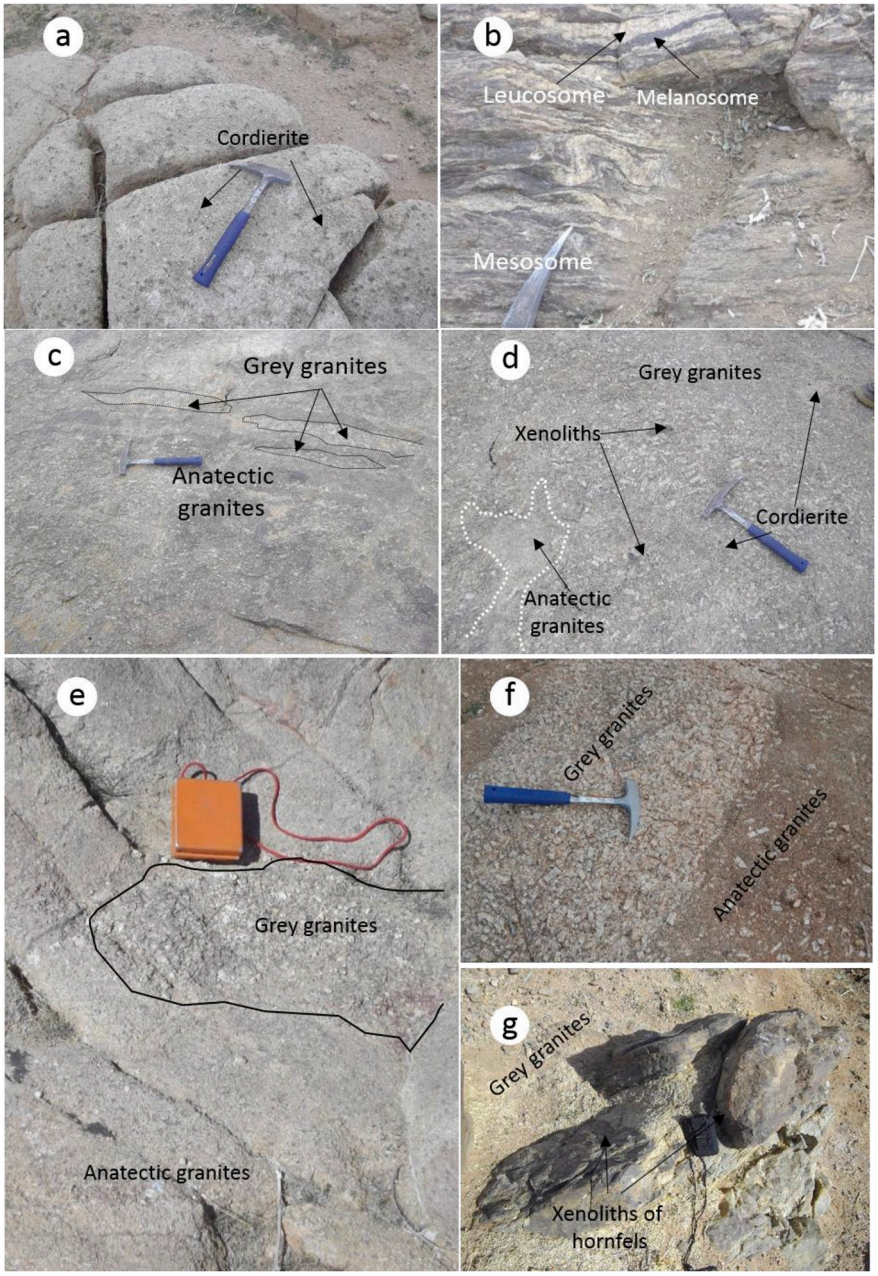

Fig. 5. Field photographs of HLA area: a) Anatectic granite spotted by cordierite megacrysts. b) Deformed layered migmatites. c, d, f and g) Features of interactions between anatectic granites and grey granites in their contact zone (mingling and mixing features) g) Hornfels xenoliths in grey granites at the contact with metamorphic aureole of the complex.

peraluminous anatectic suite. The basic to intermediate suite (gabbro-diorites and granodiorites) occurs as an aureole rimming the so-called Grey granite in the northeastern part of the inlier (El Hassir apophysis, Fig. 2) and as small plutons and veins crosscutting the intruded metasedimentary series. Gabbro-diorites display ASI and ANK ranging from 0.9 to 1.03 and 1.8–3.15 respectively (Fig. 3) and $^{87}Sr/^{86}Sr$ = 0.7052 (Clauer et al., 1980; Tisserant, 1977). Granodiorites have ASI varying from 0.85 to 1.05 and ANK from 1.65 to 2.25 (Fig. 3). The metaluminous granitic suite occurs as large plutons (the so-called Grey and Pink granites) in the western part of the inlier (Emberger, 1965; El Mouraouah, 1993; Oukemini and Bourne, 1994). They display ASI ranging from 0.95 to 1.05, ANK ranging from 1.05 to 1.45 (Fig. 3) and for the Grey granite $^{87}Sr/^{86}Sr$ equal to 0.7101 (Clauer et al., 1980; Tisserant, 1977). The peraluminous anatectic S-type suite is represented by various rock types (Table 1): i) anatectic granites and migmatites associated with the metaluminous Grey granite in the Hassan II lake area (HLA) in the southeastern part of the complex; ii) anatexites very rich in xenoliths and garnets forming a small stock (area of 2 km^2) emplaced within the metasediments east of the El Hassir apophysis; this xenolith- and cumulate-rich stock named "Colline à Essaim d'Enclaves" (CEE) or "hill swarm of enclaves" has been first recognized by El Mourouah (1993); iii) two-mica granites constituting the small plutons of Poulet and Perdreaux intruding metasedimentary rocks in the eastern part of the complex (281 Ma, Clauer et al., 1980); iv) Crd-bearing microgranites occurring as decametric to metric dykes cross-cutting the granitoids and surrounding metasediments. The peraluminous suite (Table 1 and Fig. 3) displays ASI > 1.1 and ANK varying from 1.1 to 1.95, and for the two micas-granites $^{87}Sr/^{86}Sr$ ratio of 0.7204 (Clauer et al., 1980; Tisserant, 1977).

Our study will be essentially focussed on the HLA and CEE for the definition of melting processes and their thermodynamic conditions as well as for the characterization of the emplacement mode of the two granite types (meta- and peraluminous) within the metasedimentary series.

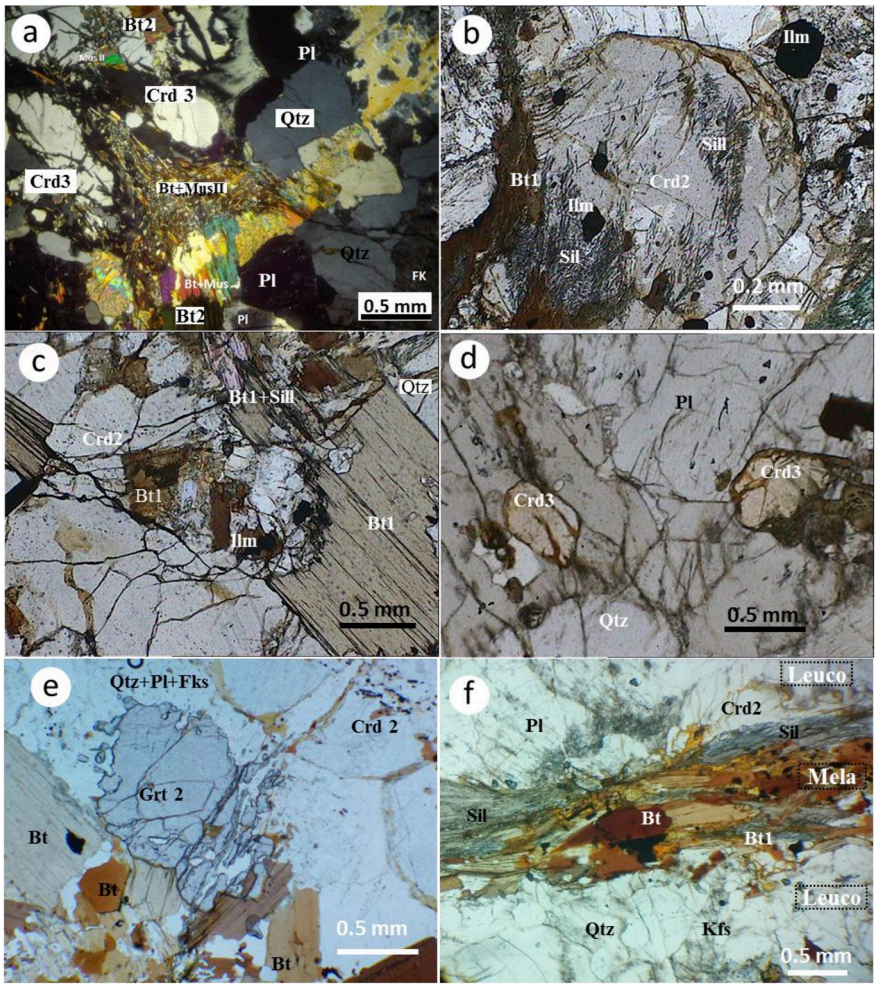

Fig. 6. Photomicrographs illustrating the textures and mineral relations in HLA anatexites: a) general texture of HLA granites. b) Association of biotite, Crd2 and sillimanite in the HLA Crd-bearing granites. c) Peritectic Crd associated wih Bt and Sil in the migmatite of the HLA zone. d) Cotectic (euhedral) Crd3 in the anatectic granite of the HLA. e) Garnet in the HLA granites. f) Adjacent leucosomes (Qtz, Kf, Pl and Bt) and melanosomes (Bi and Sil) in the migmatite of the HLA.

4. Field relationships and petrography of the peraluminous occurrences in Aouli-Mibladen complex

4.1. Anatexites of Hassan II lake area (HLA)

In the southeastern part of the Aouli-Mibladen complex, anatexites of the HLA are adjacent to the Grey granite (Fig. 2) and form a lenticular body elongated NNE-SSW, 3 km long, 2.5 km wide (Fig. 4a and b). Anatexites include cordierite and garnet bearing granites (Fig. 5a; mineral abbreviations after Kretz, 1983) and some metric to hectometric occurences of layered migmatites (Fig. 5b). The two granites, both anatectic and grey, intrude the Paleozoic metasediments with development of a contact metamorphic zone underlined by Sill, And, Crd and Bt isograds from grey granites to external part of the contact zone respectively (Figs. 2 and 4). The anatexites body is mainly composed of homogenous cordierite bearing granite surrounded by a mingling zone (100–200 m thick) defined by a mix of grey and anatectic granites (Fig. 4).

The main features (Fig. 5c to f) consist of anatectic granite layers penetrating the Grey granite and layers of Grey granite within the anatectic Crd-bearing granite. The layers (cm to m thick) show rectilinear or sinuous boundaries. Elongation of the structures (orientation of phenocrysts and lenticular bodies of Grey granites into anatectic ones) is due to flow of the two partially crystallised magmas. Hybrid zones exist between the two contrasting magmas, but these zones show limited mixing and mingling between the two granitic melts (Ghaffari and Rashidnejad-Omran, 2014; Asrat et al., 2004; Baxter and Filly, 2002). This indicates a simultaneous emplacement of the two distinct granitic melt types within the metasedimentary surrounding.

The HLA anatexites are mainly Crd-bearing. They comprise 25% of the mode for K-feldspar, plagioclase and quartz, defining the rock as a monzogranite (Figs. 3b), 10% for biotite and 12% for cordierite, with garnet as an accessory phase. Plagioclase occurs as tabular grains ranging in size from 0.4 mm to 4 mm long. K-feldspar forms large anhedral crystals (> 4 mm) enclosing plagioclase and biotite (Fig. 6a). Quartz is also anhedral and ranges in size from 0.4 to 2 mm. Biotite shows different shapes and sizes with small anhedral lamellae (< 1 mm) closely associated with cordierite and sillimanite (Fig. 6b), named Bt1 and millimetric euhedral and tabular Bt2 sections associated with feldspars and quartz (Fig. 6a). Cordierite appears as: i) subhedral to anhedral grains including biotite and sillimanite fibers and small euhedral ilmenite (Fig. 6c); ii) euhedral, globular, diamond-shaped or hexagonal millimetric grains (Fig. 6d) generally free of inclusions and participating to the main texture of the granite. Rare millimetric subhedral to euhedral garnet grains are sometimes associated with subhedral biotite and cordierite (Fig. 6e). Muscovite occurs as euhedral lamellae (~1.5 mm in size) growing on cordierite and/or biotite (Fig. 6b and d). Accessory minerals are: i) sillimanite fibers enclosed by cordierite, rarely by K-feldspar and quartz; ii) zircon enclosed by biotite; and iii) opaque minerals associated with cordierite and muscovite.

The Crd-bearing granites of Hassan II Lake Area enclose some scattered metric to decametric fragments of migmatites elongated parallel to the limits of the body. Migmatites are metatexites with two

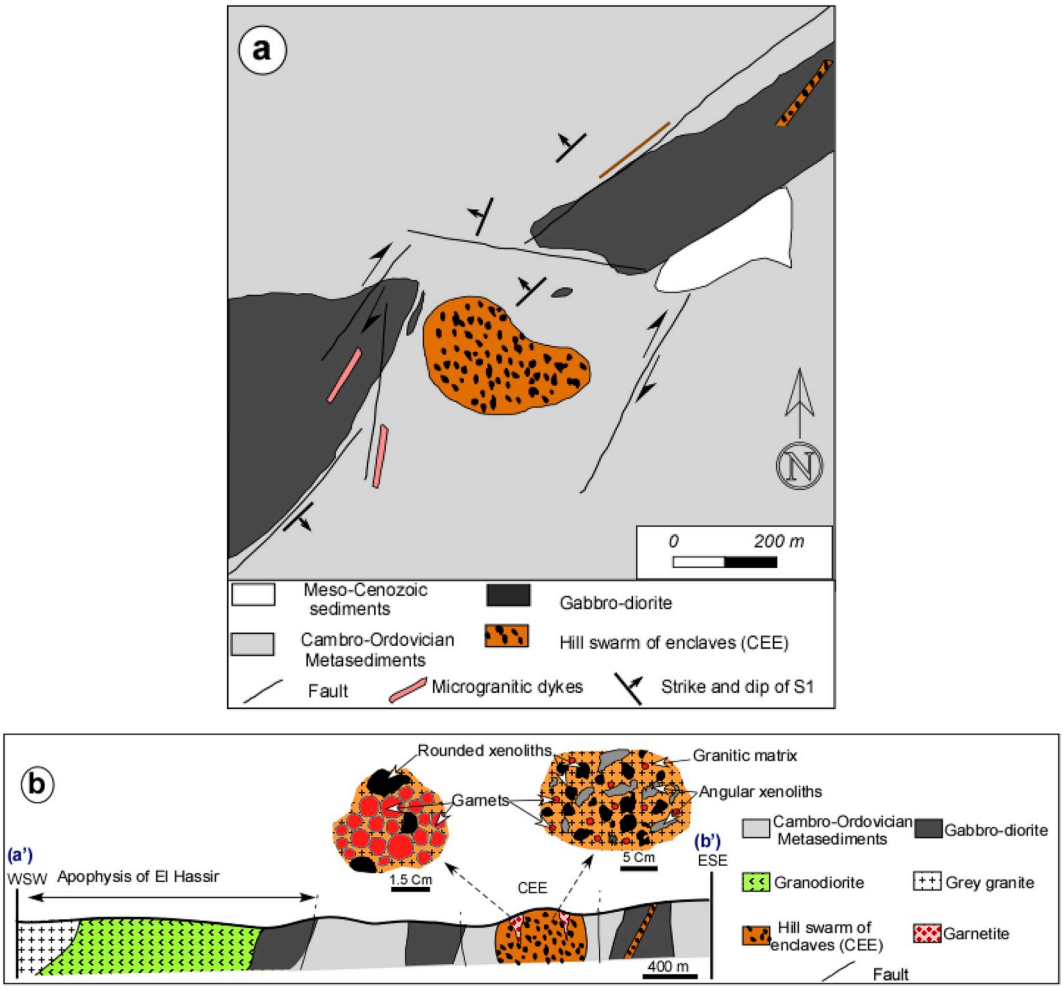

Fig. 7. a) Simplified geological map around xenolith-cumulate deposit (CEE) in El Hassir area of Aouli Mibladen complex. b) Geological section along the profile a'–b' (see, Fig. 2).

types of structure: I) stromatic structure defined by alternating layers of leucosome, melanosome and mesosome (Fig. 5b); ii) nebulitic structures and schlieren defining a transitional facies between migmatites and hosting anatectic granites.

Migmatitic leucosomes correspond to coarse-grained quartzo-feldspathic rocks with typical granitic texture (Fig. 6f). K-feldspar, plagioclase and quartz are the dominant minerals with modal proportions varying from 35 to 55%; 10–20%; and 20–30% respectively. Melanosomes are mainly composed of biotite (30–50%), sillimanite (30%), cordierite (15%) and subordinate garnet and opaque minerals (Fig. 6f). In leucosomes, biotite and cordierite arepresent in small modal proportions (≤5%). Biotite is usually euhedral, millimetric in size with a strong pleochroism when included or associated with quartz, K-feldspar and plagioclase (Fig. 6f). Anhedral biotite lamellae, with slight pleochroism are also present mainly in melanosomes with relict character. Cordierite has globular shape and dimensions sometimes up to 1 mm (Fig. 6c), and the occasionally associated garnet is subhedral to euhedral. These two latter minerals exhibit the same textural features as in anatectic granites described above.

4.2. Hill swarm of enclaves (CEE)

Located NE of the Aouli-Mibladen complex the CEE is a small (2 km^2) magmatic body (Fig. 7a and b and Fig. 8a) intruding the Paleozoic metasediments with development of a thin metamorphic aureole.

Recognized and summarily described by El Mouraouah (1993), the CEE corresponds to a leucocratic cordierite and/or garnet bearing granite including numerous xenoliths and xenocrysts of different nature, shape and size (Fig. 8b and c). Granites display a coarse-grained texture composed mainly of quartz, K-feldspar, plagioclase, biotite and in various proportions cordierite, sillimanite and garnet (see below). The garnet distribution is heterogeneous. In some areas, scattered garnet crystals represent ~9% of the modal composition. In other areas (several 10 m^2), garnet constitute more than 80% of the modal composition (Fig. 8c and d). These garnetites are composed of hundreds of subhedral to euhedral, millimetric to centimetric garnet crystals. Garnets and xenoliths display a cumulate like texture with an interstitial ("intercumulus") granite matrix (Fig. 8b to e).

Xenoliths are scattered and in a few cases can represent more than 30% of the rock (Fig. 8b). They constitute two different types. Several centimeters large, angular and tabular xenoliths correspond to the host rocks metamorphosed to sillimanite bearing hornfels and quartzite. They are concentrated near the CEE borders. The second type corresponds to rounded xenoliths with smaller sizes (< 3 cm) and variable mineralogy (Abaché and Kimba, 2011) randomly distributed within the CEE. Their main types are corundum-cordierite xenoliths, corundum-plagioclase xenoliths and garnet xenoliths (Abaché and Kimba, 2011). They correspond to transported fragments of wall rocks during magma ascent from deeper zones.

The CEE has an overall granitic composition and coarse grained texture, with 30% Qtz +25% Pl + 10% Kf + 15% Bt + 10% Crd, ≤ 9% garnet on average, and 1% Sil (Figs. 3b and 9a, b). This modal composition and texture are similar to that of HLA anatectic granites. Garnet is ubiquitous but with variable modal proportions resulting from

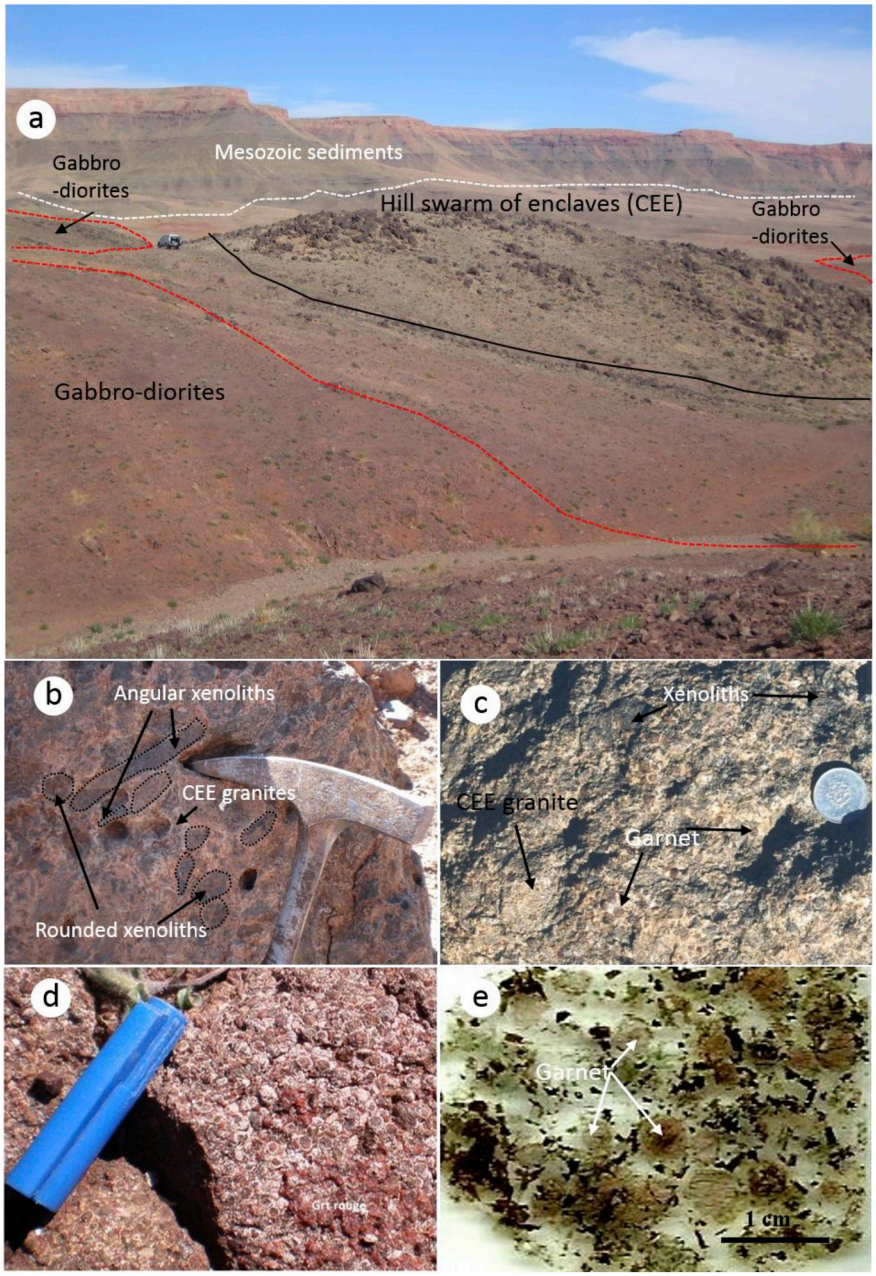

Fig. 8. a) The CEE outcrop in the NE part of Aouli-Mibladen complex. In the background, the subhorizontal Triassic (basalts and sandstones) and Liassic (limestones) unconformable cover of the Paleozoic basement. b) Variability of metasedimentary xenoliths in CEE granites c) Dark garnet crystals and xenocrysts contrasting with the leucocratic granites. d) Red garnets in CEE forming garnetites; e) Photomicrograph of the thin section, under binocular loupe, showing the high garnet concentration in the granitic groundmass (due to amalgamation).

its irregular distribution within CEE granites (see above). Secondary muscovite, chlorite and opaque minerals are common but in low modal proportions (< 1%).

Two types of garnet have been recognized in the CEE. Type 1 garnet (Grt1) is associated with cordierite and spinel in a coronitic texture. It corresponds to anhedral, rare grains, 5 mm in size enclosing sillimanite, biotite and quartz and separated from the granitic groundmass by a continuous corona of cordierite (named Crd1) with biotite and spinel inclusions (Fig. 9c). Type 2 garnet (Grt2) appears as globular megacrysts ranging from 0.2 mm to 1 cm, locally surrounded by a microcrystalline assemblage composed of quartz, plagioclase and biotite separating it from the coarse-grained granitic groundmass (Fig. 9d). These garnets are mainly euhedral and show optical zoning. In most cases, garnets show inclusion-rich cores and inclusion-free rims (Fig. 9d). Rounded and welded garnet crystals define a cumulate-like texture (Fig. 8d, e and 9e, see above). We can also observe some dislocated garnet fragments for which the original garnet shape can easily be reconstructed (Fig. 9f).

Four cordierite types are distinguished in CEE: i) Crd 1 associated with Grt1 as continuous coronas separating it from the granitic groundmass (see the paragraph above); ii) anhedral to subhedral Crd2 with biotite, sillimanite and ilmenite inclusions (Fig. 9a); iii) euhedral inclusion-free Crd3 (Fig. 9b); iv) Crd4 surrounding partially or totally Grt2 (Fig. 9g). Crd2 and Crd3 have already been observed in the HLA Crd-granite.

4.3. Microgranitic dykes

Many decametric to metric cordierite-muscovite bearing microgranite dykes crosscut all the petrographic types of the main complex as well as the metamorphic aureole in various orientations (Figs. 2, 4a and

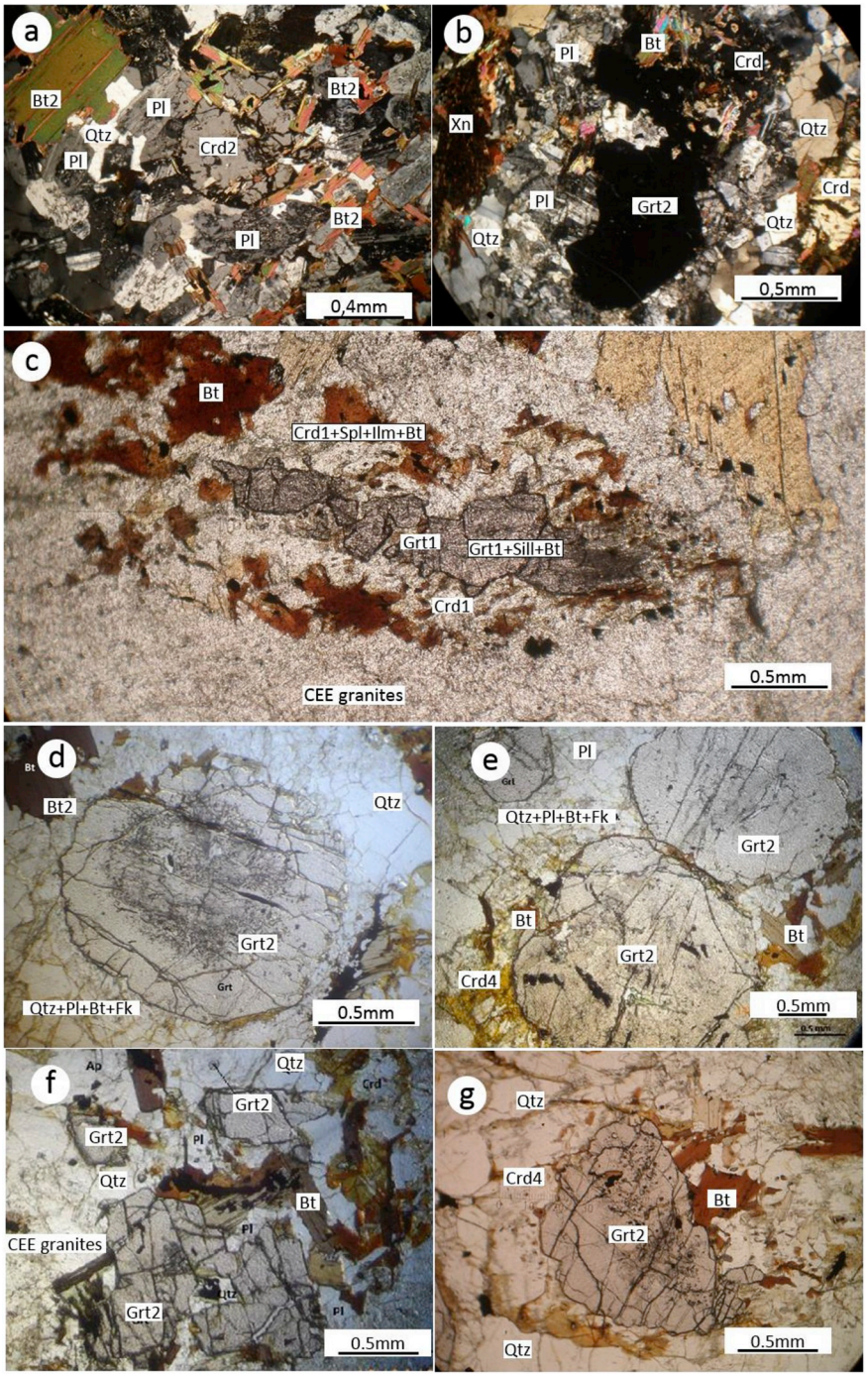

Fig. 9. Photomicrographs of different types of garnet and cordierite in the CEE anatectic granites. a and b) general texture of cordierite and garnet bearing CEE granites. c) Type 1 garnet (Grt1): anhedral relict xenocrysts of garnet separated from the granitic matrix by a continuous corona of Crd1 containing spinel, biotite, and ilmenite. d) Type 2 garnet (Grt2): surrounded by a microcrystalline assemblage composed of quartz, plagioclase and biotite showing inclusion-rich cores and inclusion-free rims. e) Rounded amalgamated Grt2 crystals in CEE granites. f) Fractured Grt2 crystals. Note also, at the garnet contact, the development of biotite and the relictual character of enclosed Ilm g) Garnet 2 mantled by cordierite 4 aureole.

4b and 8a and Fig. 10a). They are small-grained leucocratic rocks of monzogranitic composition (Fig. 3b). Minerals are mostly K-feldspar (30%), quartz (30%), plagioclase (25%) and primary muscovite with minor biotite, cordierite and sillimanite (Fig. 10b).

4.4. Two-mica granites

Two-mica granites constitute two kilometer-sized stocks named Poulet and Perdreaux (Figs. 2 and 4b) crosscutting the metamorphic aureole of the Aouli-Mibladen complex in its eastern part, making them completely isolated from the rest of the complex. They consist mostly of medium-grained muscovite-monzogranite (Fig. 3b) containing less than 2% biotite. Primary muscovite, with up to 10% modal proportions, occurs as large crystals up to 1.5 mm length (Fig. 10c). Microcline (20%) occurs as large anhedral crystals (> 4 mm) enclosing plagioclase and biotite. Plagioclase (20–30 vol %) shows normally zoned euhedral crystals 0.5–2 mm in size. Sillimanite fibers and small garnet crystals or fragments are sporadically distributed in this petrographic type (Fig. 10d).

5. Mineral chemistry

5.1. Feldspars

In HLA and CEE anatectic granites plagioclase displays two different compositions. Plagioclase associated with euhedral Bt, Qtz and Kfs in granitic coarse-grained textures (Pl1) has an overall oligoclase-andesine composition but shows a discrete normal zoning ranging from An_{36} in the core to An_{31-33} in the rim. Plagioclase associated with cordierite 2

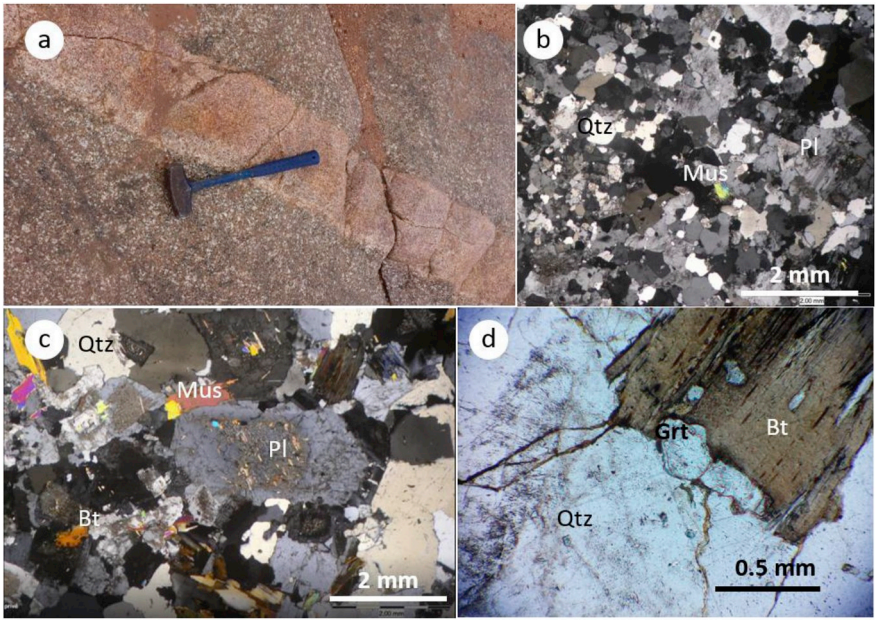

Fig. 10. a) Microgranite dyke crosscutting the grey granite in HLA. b and c) Photomicrographs showing the main forming minerals and textures of Crd-bearing microgranitic dykes and two mica granite of Poulet stock respectively; d) garnet fragments enclosed in two-mica granites minerals.

Table 2
Major elements compositions and structural formulae (8 oxygens) of representative feldspars of Aouli-Mibladen S-type suite.

Mineral	Plagioclase										K-feldspar				
Rock type	HLA migmatite			HLA anatectic granite				CEE granite			HLA migmatite		HLA anatectic granite		
Sample	MIGT1		MIGT2	GCdr1				CEE101B			MIGT2		GCdr1		GCdr2
SiO_2	63.85	64.01	63.43	68.94	64.19	64.29	67.22	58.99	58.92	59.98	64.97	64.87	64.14	64.81	64.60
TiO_2	0.01	0.00	0.00	0.01	0.00	0.00	0.00	0.00	0.00	0.00	0.02	0.00	0.00	0.00	0.00
Al_2O_3	21.77	22.19	22.48	19.41	21.61	22.13	19.95	25.79	25.43	25.33	18.43	18.48	18.39	18.79	17.98
FeO	0.10	0.08	0.05	0.03	0.03	0.03	0.01	0.15	0.10	0.05	0.08	0.01	0.05	0.02	0.01
MnO	0.00	0.02	0.00	0.00	0.00	0.00	0.05	0.00	0.00	0.00	0.00	0.00	0.00	0.04	0.00
MgO	0.00	0.01	0.00	0.03	0.00	0.00	0.00	0.00	0.00	0.00	0.00	0.00	0.00	0.00	0.00
CaO	3.31	3.38	4.08	0.53	3.08	3.44	1.03	7.47	7.25	6.86	0.06	0.00	0.04	0.00	0.08
Na_2O	9.06	8.98	8.67	10.98	9.79	9.22	10.70	7.36	7.52	7.60	2.90	2.38	0.75	1.49	1.72
K2O	0.40	0.51	0.27	0.11	0.43	0.55	0.11	0.08	0.04	0.05	12.77	13.33	15.80	14.89	14.46
Total	98.53	99.25	99.05	100.08	99.21	99.86	99.17	99.84	99.26	99.87	99.44	99.23	99.30	100.20	98.98
Si	2.87	2.86	2.84	3.03	2.85	2.85	2.98	2.64	2.65	2.68	2.98	2.99	2.98	2.97	3.00
Al	1.15	1.17	1.19	1.00	1.13	1.16	1.04	1.36	1.35	1.33	1.00	1.01	1.01	1.02	0.98
Ca	0.16	0.16	0.20	0.02	0.15	0.16	0.05	0.36	0.35	0.33	0.00	0.00	0.00	0.00	0.00
Na	0.79	0.78	0.75	0.93	0.84	0.79	0.92	0.64	0.65	0.66	0.26	0.21	0.07	0.13	0.15
K	0.02	0.03	0.02	0.01	0.02	0.03	0.01	0.00	0.00	0.00	0.75	0.78	0.94	0.87	0.86
tot. cat.	5.00	5.00	5.00	5.00	5.00	5.00	5.00	4.99	5.00	5.00	5.00	5.00	5.00	5.00	5.00
An	16.42	16.69	20.32	2.57	14.46	16.56	5.03	35.76	34.67	33.20	0.27	0.00	0.21	0.00	0.37
Ab	81.21	80.33	78.06	96.79	83.17	80.30	94.35	63.76	65.09	66.52	25.57	21.31	6.71	13.19	15.21
Or	2.37	2.98	1.62	0.63	2.37	3.14	0.62	0.48	0.24	0.28	74.17	78.69	93.09	86.81	84.42

and sillimanite (Pl2) is more calcic with an andesine-labrador composition (An_{37} to An_{52}) and a normal zoning with a labradorite core (An_{52} to An_{60}) and an andesitic rim (An_{37}).

Alkali feldspars are mainly orthoclase in migmatites and anatectic granites including those of CEE with microperthitic structure. Microcline is the dominant alkali feldspar in microgranite dykes and two-mica granites. Their chemical compositions vary from Ab_{26} Or_{74} to Ab_7 Or_{93} (Table 2).

5.2. Biotite

Two types of biotite (Bt1 and Bt2) characterize the peraluminous suite of Aouli-Mibladen (Table 3 and Fig. 11). In HLA and CEE anatectic granites, Bt1 is included as relictual grains in the subhedral cordierite with sillimanite and ilmenite. Bt1 shows moderate Mg and low Ti contents, with X_{Fe} (Fe/[Fe + Mg]) varying from 0.5 to 0.69 and Ti from 0.3 to 0.4 apfu (22 oxygens; Table 3). Bt2 in migmatite leucosomes, anatectic granites and two-mica microgranites corresponds to Fe-rich biotites (X_{Fe} higher than 0.65) with lower contents of Ti, less than 0.3 apfu.

5.3. Cordierite

Cordierite analyses are given in Table 4. Their textural and chemical characters are summarized in Table 7. Four cordierite types exist in the Aouli-Mibladen anatexites: i) in CEE, the first type (Crd1) corresponds to the cordierite coronas around Grt1 and associated with spinel. Its X_{Fe}

Table 3
Major elements compositions and structural formulae (22 oxygens) of representative biotite types.

Mineral	Bt1								Bt2											
Rock type	CEE granite						HLA granite		CEE granite	HLA granite	HLA Migmatites								Two-mica granite	
Sample	CEE101B		CEE8				AB53		CEE101B	GCdr2	MIGT1						MIGT2		GMP	
SiO2	34.35	34.33	34.60	34.98	36.14	34.01	35.02	35.57	33.69	33.64	34.20	33.67	33.52	34.52	34.36	34.25	33.96	33.73	34.48	34.62
TiO2	2.49	2.56	1.11	3.83	2.48	1.61	2.28	2.58	3.05	2.68	2.56	3.03	3.01	2.47	2.21	2.29	2.39	2.56	2.58	2.49
Al2O3	19.41	19.60	21.93	18.44	19.65	21.74	19.77	18.74	19.72	18.47	19.12	18.36	18.29	18.41	18.66	18.49	18.45	18.47	18.66	18.75
FeO	20.81	20.94	20.44	21.40	18.51	19.91	20.09	20.19	24.20	24.87	23.29	24.33	24.13	23.79	23.18	23.38	23.15	24.20	21.46	21.46
MnO	0.31	0.26	0.27	0.09	0.04	0.03	0.63	0.34	0.21	0.44	0.09	0.11	0.15	0.13	0.17	0.20	0.20	0.18	0.62	0.80
MgO	7.77	7.99	8.25	8.27	9.99	8.31	6.46	6.97	5.51	4.06	5.23	4.67	4.82	5.22	5.46	5.47	5.33	5.40	5.76	5.85
CaO	0.06	0.00	0.14	0.14	0.06	0.05	0.00	0.04	0.00	0.02	–	–	–	–	–	0.01	–	–	0.00	0.00
Na2O	0.19	0.16	0.17	0.25	0.14	0.02	0.17	0.19	0.17	0.19	0.18	0.24	0.16	0.20	0.16	0.22	0.23	0.24	0.08	0.05
K2O	9.37	9.07	8.61	8.88	8.94	8.83	9.13	8.88	8.97	9.42	9.33	9.44	9.56	9.69	9.86	9.44	9.56	9.52	9.85	9.52
BaO	–	–	0.08	0.04	0.05	0.00			–	0.05	–	0.08	0.03	–	0.08	0.05	0.04	–	0.01	0.13
F	–	–	–	–	–	–			–	0.35	–	–	0.87	–	0.52	0.63	0.97	0.35	0.84	0.67
Cl	–	–	–	–	–	–			–	0.12	–	0.09	0.14	–	0.09	0.10	0.08	0.12	0.01	0.00
Cr2O3	0.15	0.14	0.12	0.02	0.03	0.12			0.06	0.05	0.24	0.10	0.14	0.07	0.04	0.12	0.30	0.04	0.05	0.00
Total	96.76	96.92	97.40	98.21	97.58	96.44	93.55	93.50	97.41	94.36	94.23	94.10	94.84	94.49	94.78	94.65	94.67	94.81	94.39	94.34
Si	5.31	5.28	5.24	5.32	5.41	5.20	5.41	5.48	5.24	5.37	5.36	5.35	5.34	5.42	5.40	5.40	5.39	5.34	5.42	5.42
Al	3.53	3.56	3.92	3.30	3.46	3.92	3.60	3.40	3.62	3.48	3.53	3.44	3.44	3.40	3.46	3.44	3.45	3.44	3.46	3.46
Ti	0.29	0.30	0.13	0.44	0.28	0.19	0.26	0.30	0.36	0.32	0.30	0.36	0.36	0.29	0.26	0.27	0.29	0.30	0.31	0.29
Fe	2.69	2.70	2.59	2.72	2.31	2.55	2.60	2.60	3.15	3.32	3.05	3.23	3.22	3.12	3.05	3.08	3.07	3.20	2.82	2.81
Mn	0.04	0.03	0.03	0.01	0.00	0.00	0.08	0.04	0.03	0.06	0.01	0.02	0.02	0.02	0.02	0.03	0.03	0.02	0.08	0.11
Mg	1.79	1.83	1.86	1.87	2.23	1.90	1.49	1.60	1.28	0.97	1.22	1.11	1.15	1.22	1.28	1.29	1.26	1.27	1.35	1.37
Ca	0.01	0.00	0.02	0.02	0.01	0.01	0.00	0.01	0.00	0.00	–	–	–	–	–	0.00	–	–	0.00	0.00
Na	0.06	0.05	0.05	0.07	0.04	0.01	0.05	0.06	0.05	0.06	0.06	0.07	0.05	0.06	0.05	0.07	0.07	0.07	0.02	0.01
K	1.85	1.78	1.66	1.72	1.70	1.72	1.80	1.74	1.78	1.92	1.87	1.92	1.94	1.94	1.98	1.90	1.93	1.92	1.97	1.90
tot. cat.	15.56	15.53	15.51	15.48	15.45	15.49	15.29	15.22	15.50	15.50	15.40	15.50	15.52	15.47	15.50	15.48	15.49	15.56	15.43	15.38
X_{Fe}	0.60	0.60	0.58	0.59	0.51	0.57	0.64	0.62	0.71	0.77	0.71	0.75	0.74	0.72	0.70	0.71	0.71	0.72	0.68	0.67

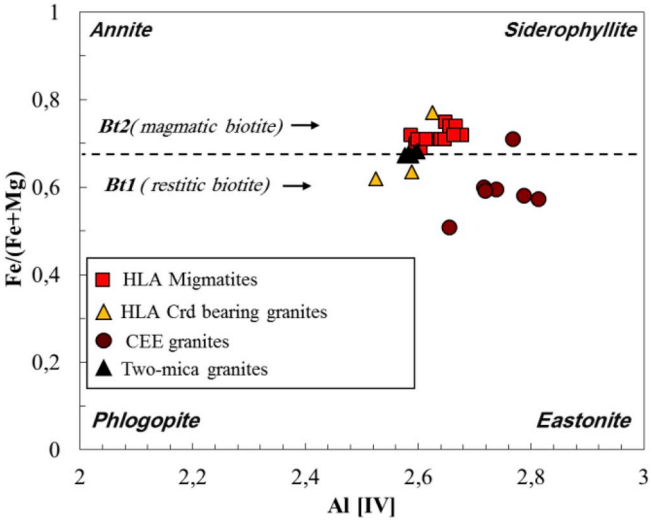

Fig. 11. Biotite compositions of the peraluminous suite of the Aouli Mibladen granitic complex in the diagram Fe/(Fe + Mg) vs Al IV (Guidotti, 1984).

ratio is less than 0.43; ii) in HLA and CEE, anhedral Crd2, associated with relict Bt1, sillimanite and ilmenite has the highest MgO contents (from 4.7% to 7.6%) and the lowest FeO contents (from 9.3% wt to 10.7%), displaying an X_{Fe} ratio of 0.37 on average; iii) euhedral globular Crd3 in migmatite leucosomes, in Crd granites as well as those from microgranitic veins are Fe-richer, displaying MgO contents varying from 1.4% to 4.7% and FeO from 4.2% to 13.8% with an X_{Fe} ratio of 0.6; iv) Crd4 coronas rimming Grt2 in CEE granites exhibit an X_{Fe} close to 0.57.

5.4. Ilmenite

Ilmenite, the major opaque mineral in migmatites, Crd-granites and CEE granites is closely associated with relict Bt1 and subhedral Crd2. It has a composition of 53–54.6% TiO_2, 41.5% FeO and nearly 3.9% MnO (Table 5).

5.5. Spinel

Spinel as small inclusions in Crd1 coronas around Grt1 shows (Table 5) a hercynite composition with more than 37% FeO and less than 2.5% MgO. Alumina content is ~58% and Cr_2O_3 and TiO_2 contents are close to or below the detection limit.

5.6. Garnet

Representative garnet analysis are given in Table 6.

Garnet 1: The major-element chemisty of Grt1 has been done in spot mode because of its small size and relict character. It appears homogeneous with an average composition of $Alm_{72.78}$, $Sps_{14.75}$, $Prp_{9.17}$, $Grs_{3.28}$.

Garnet 2: In the CEE, both isolated and amalgamated Grt2 are predominantly almandine (Alm), with minor amounts of pyrope (Prp) and subordinate amounts of spessartine (Sps), and grossular (Gr). Andradite (Adr) and uvarovite (Uv) contents are negligible. Generally, they show different zoning profiles with an overall compositional range of $Alm_{67.5\text{-}77.3}$, $Prp_{4.6\text{-}19.5}$, $Gr_{2.5\text{-}16.3}$, $Sps_{3.7\text{-}15.1}$ (Table 6).

Analysing chemical maps and zoning profiles of CEE Grt2 allows to define two main subtypes of zoning with few variations within each subtype.

Garnet 2A shows three domains: core, inner rim and outer rim (see sketch in Figs. 12a and 13a and Table 6). In chemical maps, garnet cores are euhedral and show prograde growth patterns for MgO, CaO and MnO (Figs. 12b and 13b). They are separated from inner rim by an irregular and sinuous border (Figs. 12b and 13b) evidenced by CaO, MnO and MgO chemical maps. Toward the rim MnO, FeO and CaO are irregularly enriched and MgO depleted. The outer rim is marked by a slight reverse evolution at its contact with the granitic groundmass. Transect zoning profiles (Figs. 12a and 13a) provide more detail on element behaviour. Grt2A garnets are characterized by symmetric, bell-shaped profiles of spessartine, grossular and X_{Fe} and reverse bell-shaped profiles for pyrope and almandine. However, in some garnets, the growth zoning is followed by a narrow rim, with a renewed increase in spessartine, grossular and X_{Fe}, and a decrease in pyrope, typical for partial Grt resorption.

Garnet 2B show a more complex zoning indicating development in, at least, three main steps. In this case four domains are distinguished: inner core, outer core, internal rim and outer rim (Fig. 14a). Analysing first the zoning profiles (Fig. 14a) allows to highlight: i) the flat shape of inner core contents of the four end-members and X_{Fe}; ii) the bell shaped profile in outer cores corresponding to an increase of Sps, Grs and X_{Fe} toward the rim (similar to the rims of Grt2A) reaching a maximum, followed by a strong decrease in these components; iii) the slight increase in these components at the internal rim followed by their increase at the contact with the granitic matrix (outer rim); iv) a reverse trend from core to rim for Prp. Its flat shape in the inner core is followed by a reverse bell shaped profile in the outer core and then a slight decrease at the contact with the granitic groundmass.

In the small Grt2B grain (Fig. 15), the inner core is small, 500 µm against 2500 µm for the garnet analysed in Fig. 13, but the same chemical trends can be noted. Element maps (Fig. 15b) display, as for Grt2A, the sinuous and irregular border separating the outer core and internal rim of this garnet grain.

Where two garnet grains are in contact, they show independent inner zoning, whereas their rims have common zoning patterns (Fig. 13b). This feature, well shown in MgO chemical map, indicates that their cores have grown independantly, while their rims were formed after the amalgamation of garnet grains and suggests that these garnets have a separate story before becoming amalgamated.

5.7. Comparison between garnet compositions and zoning

Grt2A cores and Grt2B outer cores share the same compositions marked by bell shaped profiles for Sps, Grs and X_{Fe} and reverse bell-shaped profiles for Prp, indicating that they most likely develop under similar chemical and physical conditions.

Inner rims of both garnets 2A and 2B are separated from their cores by a very sinuous border corresponding to a dissolution/resorption episode (Figs. 1, 12 and 135b). Compositions and end-members evolution of these inner rims are also similar (Fig. 16). They underline the same reprecipitation process at the contact of crystallizing melt (see above). Finally, the external rims show different and variably marked chemical evolutions. They correspond to the interaction, in their direct contact, between garnet rims and different minerals of the granitic groundmass under subsolidus conditions.

Grt1 and the inner core of Grt2B have common petrographic characters i.e, no zonation and Sill, Bt and Qtz inclusions. They correspond probably to the same garnet generation despite the fact that they have different chemical compositions in oxide contents as well as on their end-members ratios (Grs/Prp, Grs/Alm and Alm/Prp, Fig. 16). Theses differences would have been probably due to reequilibrations during anatexis and/or subsolidus processes depending on metamorphic conditions, crystal sizes and related diffusion rates of elements.

6. Mineral reactions

Anatexites of Aouli-Mibladen complex exhibit some textural relationships typical of well known reaction textures and mineral reactions. The most important ones are:

Table 4
Major elements compositions and structural formulae (18 oxygens) of cordierite types in Aouli-Mibladen S-type rocks.

Mineral	Crd1		Crd2										Crd3										Crd4
Rock type	Aureole around Grt 1		HLA Anatectic granite					CEE granite					HLA Migmatites										CEE granite
Sample	CEE8		AB 53					CEE102					MIGT1					MIGT2					CEE21
SiO2	48.06	47.92	47.47	47.25	47.26	47.56	47.52	48.00	48.28	48.57	47.97	48.96	47.11	46.52	46.85	46.94	46.75	47.38	47.45	47.47	46.86	47.07	47.34
TiO2	0.00	0.07	0.00	0.03	0.00	0.00	0.00	0.00	0.00	0.00	0.15	0.04	0.00	0.00	0.00	0.00	0.01	0.00	0.00	0.00	0.00	0.00	0.00
Al2O3	34.04	32.91	32.45	32.06	33.25	33.99	33.56	33.25	32.81	32.84	33.14	33.14	31.34	31.28	30.97	31.17	31.46	31.23	31.70	31.28	31.19	30.94	36.80
FeO	9.26	9.74	7.89	7.95	7.86	7.74	7.83	9.33	9.68	9.80	9.68	9.61	13.54	13.88	13.44	13.32	13.62	13.09	13.54	13.28	13.39	13.33	10.68
MnO	0.00	0.41	0.22	0.17	0.00	0.16	0.03	0.32	0.00	0.44	0.22	0.28	0.28	0.29	0.22	0.31	0.30	0.40	0.29	0.38	0.33	0.32	0.24
MgO	7.85	7.25	7.96	7.86	7.69	7.68	7.85	7.27	7.33	7.30	7.65	7.65	4.38	4.56	4.40	4.73	4.43	4.47	4.42	4.59	4.65	4.53	4.68
CaO	0.10	0.07	0.04	0.01	0.02	0.02	0.01	0.04	0.04	0.05	0.00	0.00	0.03	0.09	0.01	0.01	0.00	0.00	0.01	0.02	0.00	0.00	0.01
Na2O	0.17	0.10	0.21	0.10	0.07	0.15	0.68	0.21	0.19	0.22	0.00	0.13	0.35	0.38	0.35	0.36	0.35	0.32	0.31	0.29	0.26	0.32	0.09
K2O	0.00	0.01	0.08	0.73	0.07	0.05	0.03	0.00	0.00	0.00	0.00	0.01	0.01	0.00	0.02	0.02	0.02	0.03	0.05	0.04	0.00	0.03	0.02
Total	99.47	98.49	96.32	96.15	96.22	97.35	97.51	98.41	98.33	99.24	98.81	99.82	97.04	97.03	96.51	96.86	96.93	96.97	97.78	97.43	96.86	96.85	99.85
Si	4.92	4.97	4.96	4.99	4.96	4.94	4.94	4.97	5.00	5.00	4.95	5.00	5.05	5.00	5.06	5.04	5.02	5.07	5.04	5.06	5.03	5.06	4.84
Al	4.10	4.02	4.13	3.99	4.11	4.16	4.11	4.05	4.00	3.98	4.03	3.99	3.96	3.96	3.94	3.94	3.98	3.94	3.97	3.93	3.95	3.92	4.44
Fe2	0.79	0.84	0.64	0.70	0.69	0.67	0.68	0.81	0.84	0.84	0.84	0.82	1.21	1.25	1.21	1.19	1.22	1.17	1.20	1.18	1.20	1.20	0.91
Mn	0.00	0.04	0.01	0.02	0.00	0.01	0.00	0.03	0.00	0.04	0.02	0.02	0.03	0.03	0.02	0.03	0.03	0.04	0.03	0.03	0.03	0.03	0.02
Mg	1.20	1.12	1.22	1.24	1.20	1.19	1.22	1.12	1.13	1.12	1.18	1.16	0.70	0.73	0.71	0.76	0.71	0.71	0.70	0.73	0.75	0.73	0.71
Ca	0.01	0.01	0.01	0.00	0.00	0.00	0.00	0.00	0.00	0.01	0.00	0.00	0.00	0.01	0.00	0.00	0.00	0.00	0.00	0.00	0.00	0.00	0.00
Na	0.03	0.02	0.03	0.02	0.01	0.03	0.14	0.04	0.04	0.04	0.00	0.03	0.07	0.08	0.07	0.07	0.07	0.07	0.06	0.06	0.05	0.07	0.02
tot. cat.	11.05	11.03	11.00	11.07	10.99	11.00	11.08	11.03	11.02	11.03	11.01	11.02	11.01	11.06	11.01	11.03	11.03	11.00	11.01	11.01	11.02	11.01	10.95
X_{Fe}	0.40	0.43	0.35	0.37	0.36	0.37	0.36	0.42	0.43	0.43	0.42	0.41	0.63	0.63	0.63	0.61	0.63	0.62	0.63	0.62	0.62	0.62	0.56

Table 5
Major elements compositions and structural formulae of spinels (4 oxygens) and ilmenite (3 oxygens).

Rock type	CEE granite				
Mineral	Spinel			Ilmenite	
Sample	CEE8			CEE-3-3	
SiO2	0.00	0.02	0.01	0.25	0.00
TiO2	0.00	0.00	0.00	53.45	54.66
Al2O3	57.94	58.44	57.84	0.73	0.01
FeO	38.40	37.08	37.15	41.48	41.43
MnO	0.31	0.56	0.50	3.48	3.91
MgO	1.52	2.37	2.33	0.10	0.05
CaO	0.00	0.00	0.00	0.05	0.00
Na2O	0.00	0.00	0.00	0.05	0.00
K2O	0.00	0.00	0.00	0.00	0.00
Total	98.23	98.53	97.89	99.57	100.1
Si	0.00	0.00	0.00	0.01	0.00
Al	1.99	1.99	1.98	0.02	0.00
Ti	0.00	0.00	0.00	1.02	1.04
Fe2	0.93	0.88	0.89	0.88	0.88
Mn	0.01	0.01	0.01	0.07	0.08
Mg	0.07	0.10	0.10	0.00	0.00
tot. cat.	2.99	2.99	2.98	2.00	2.00
X_{Fe}	0.93	0.90	0.90	1.00	1.00

6.1. Crd1-Spl corona around Grt1

The formation of this type of corona has already been observed by Álvarez-Valero et al. (2007) and Álvarez-Valero and Waters (2010) in metasedimentary xenoliths embedded and transported by lavas en route to the surface in the Neogene Volcanic Province, SE Spain. These authors have shown that the corona resulted from the reaction (Álvarez-Valero et al., 2007):

Grt + Sil + Bt + Pl = Spl + Crd + Kfs + Melt

By analogy with the Spanish occurrence, one can consider that the formation of coronas around Grt1 also took place under partial melting conditions. Therefore, Grt1 crystallization is prior with early anatectic processes.

6.2. Biotite dehydration melting reactions

Pelitic schists around Aouli-Mibladen complex have undergone partial melting processes. Migmatites, anatectic granites and CEE granitic groudmass are the expressions of the partial melting and the crystallization of granitic melts. Three mineral types coexist in these rocks: i) restitic minerals including mainly biotite 1 and sillimanite and; ii) peritectic minerals such as Crd2, Grt2 and ilmenite. Reaction textures clearly demonstrate the involvement of biotite in the melting reactions (Fig. 6b and c) and iii) minerals coming from the crystallization of granitic melts defining the coarse-grained textures of leusosomes and anatectic granites, i.e. plagioclase, quartz, K-feldpspar, Crd3 (Fig. 6d), Bt2 and accessory minerals; Three well known dehydration melting reactions can be invoked in this respect (Thompson, 1982; Carrington and Harley, 1995; Spear et al., 1999):

Reaction 1 forming Crd 2: Bt1 + Sill + Qtz = Crd2 + Kf + Melt

This reaction is evidenced by textural relations showing corroded relict Ti-poor and relatively Mg-rich Bt1 and Sill enclosed or surrounded by anhedral low-X_{Fe} Crd2 in migmatite melanosomes and in some Crd-granites schlierens (see Fig. 6b and c). Ilmenite is frequently present in the reaction site. Melt is represented by quartzo-feldspathic assemblages associated with magmatic Bt2.

Reaction 2 forming Grt2: Bt1 + Sill + Qtz = Grt2 + Kf + Melt

This reaction can explain garnet growth during partial melting processes. This situation is rarely observed *in situ* (Figs. 6e and 9b). In some cases garnet is associated with cordierite types defined above. Therefore, another well-known reaction may represent the whole of the melting process (Spear et al., 1999):

Reaction 3 forming both Crd2 and Grt2: Bt1 + Sill + Qtz = Crd2 + Grt2 + Kf + Melt

This overall reaction is a synthesis of the two previous ones. Each reaction can take place in the appropriate whole rock composition under specific *P-T* conditions (Thompson, 1982; Carrington and Harley, 1995). This fits petrographic observations showing that peritectic cordierite and garnet are frequently associated in HLA and CEE areas.

6.3. Back reactions

In contrast with the previous melt-producing reactions, some textural features seem to be related to retrograde reactions some of which may correspond to melt-consuming-reactions too (Kriegsman and Alvarez-Valero, 2010). At least, two of them are represented in Aouli-Mibladen anatexites.

Cordierite coronas around Grt2: Grt2 grains are frequently surrounded by a continuous or discontinuous cordierite aureole (Crd4) as shown in Fig. 9g. Biotite 1, residual zircon and sillimanite fibers are often enclosed in cordierite. Such reaction texture correspond to the following simplified metamorphic reaction:

Grt2 + Sill + Qtz + H_2O = Crd

Crd4 development around garnet is typical of retrograde reaction taking place during decompression (Yardley, 1989; Aranovich and Podlesski, 1983).

Biotite nucleation on ilmenite: In many cases, as on Fig. 9f, we can note that, at the contact of Grt2 grains, ilmenite showing a relictual character is enclosed in biotite. Since ilmenite is a pertitectic phase produced by biotite dehydration melting reaction (see above), such textural features may indicate that biotite nucleates on this ilmenite following the melt consuming reaction:

Grt2 + Ilm + Melt = Bt + Crd + Qtz + H_2O

7. Summary and petrogenetic interpretations

In the Aouli-Mibladen granitic complex, the Hassan II lake area (HLA) is constituted of a large body of mainly Crd-bearing granites and migmatites with minor Grt. The CEE is made of Crd-bearing granites containing numerous amalgamated garnet grains and xenoliths characterized by cumulate-like texture. The typical mineral association of the whole of this anatectic rocks is: Qtz + Pl + Bt + Kfs + Sill ± Crd2 ± Grt2 ± Ilm. On a textural and chemical basis, two types of biotite, two types of garnet and four types of cordierite are distinguished (see below). Tables 7 and 8 summarize the petrographic and chemical characters of studied anatexites with special emphasis on different cordierite and garnet types, defined above as well as the nature, origin and PT conditions of these two key minerals growth.

Analysing the mineral associations and the texturally deduced reactions, it appears that biotite dehydration melting is the main reaction producing anatectic melts. Bt1 and sillimanite are frequently restitic, while Crd2 and Grt2, as described above, are the main peritectic ferromagnesian phases. K-feldspar and ilmenite are also peritectic phases that balance K and Ti, respectively, released from the reactant Bt1. Subsequent melt crystallization leads to the formation of coarse-grained leucosomes and anatectic granitic rocks consisting of cotectic Bt2, cotectic Crd3, plagioclase, K-feldspar and quartz. Crd4 surrounding Grt2 belongs to back reaction that took place during retrogression.

Some particular textural features show the presence of Grt1 forming single crystals sourrounded by Crd1 coronas containing Spl or included in the internal cores of pertitectic Grt2B. This garnet do not have direct

Table 6
Major elements compositions and structural formulae (12 oxygens) of representative garnets of Aouli-Mibladen anatexites.

	CEE8/Grt1			CEE3-3-C1/Grt2A reported on Fig. 12																
Spots	1	2	3	Outer rim	Inner rim	Core												Inner rim		Outer rim
				1	8	12	22	31	40	59	69	76	89	93	97	99	105	106	108	109
SiO2	37.11	37.13	37.12	37.40	37.66	37.86	37.42	37.35	37.08	37.21	37.30	37.40	37.25	37.44	37.25	37.50	37.76	38.02	37.08	37.81
TiO2	0.00	0.00	0.02	0.12	0.03	0.04	0.02	0.03	0.06	0.07	0.10	0.21	0.03	0.04	0.01	0.03	0.06	0.06	0.05	0.02
Al2O3	21.36	21.54	21.03	21.13	21.07	21.42	21.21	20.92	20.92	21.02	20.90	21.38	20.94	20.92	21.39	21.38	21.43	21.58	21.47	21.29
FeO	32.47	32.58	33.24	34.34	33.02	33.08	34.19	33.64	32.72	31.63	32.27	32.74	33.46	34.53	34.63	34.16	32.64	33.60	34.21	34.46
MnO	6.60	6.71	6.37	3.03	2.82	2.86	4.19	4.97	5.85	6.61	6.31	6.08	4.31	4.02	3.30	2.81	2.38	2.76	2.77	3.25
MgO	2.62	2.30	2.03	2.82	4.16	4.34	3.02	2.16	1.69	1.22	1.33	1.49	2.41	2.95	3.56	3.95	4.83	4.60	3.98	3.41
CaO	1.14	1.12	1.20	1.96	1.69	1.81	1.31	2.29	2.89	3.47	3.16	2.98	1.93	1.27	1.09	1.11	1.73	1.27	1.24	1.32
Na2O	0.00	0.00	0.00	0.02	0.02	0.02	0.00	0.01	0.00	0.00	0.00	0.02	0.03	0.03	0.02	0.03	0.00	0.00	0.03	0.01
K2O	0.00	0.00	0.00	0.00	0.01	0.02	0.01	0.04	0.00	0.02	0.00	0.02	0.00	0.00	0.01	0.01	0.01	0.00	0.02	0.00
Cr2O3	0.02	0.04	0.02	0.07	0.00	0.02	0.02	0.01	0.03	0.04	0.00	0.02	0.01	0.01	0.00	0.01	0.00	0.00	0.03	0.00
Total	101.3	101.4	101.0	100.9	100.5	101.5	101.4	101.4	101.2	101.3	101.4	102.3	100.4	101.2	101.3	101.0	100.8	101.9	100.9	101.6
Si	2.97	2.97	2.99	2.99	3.00	2.99	2.99	2.99	2.98	2.99	3.00	2.97	3.00	3.00	2.97	2.98	2.98	2.98	2.96	3.00
Ti	0.00	0.00	0.00	0.01	0.00	0.00	0.00	0.00	0.00	0.00	0.01	0.01	0.00	0.00	0.00	0.00	0.00	0.00	0.00	0.00
Al	2.02	2.03	2.00	1.99	1.98	1.99	1.99	1.98	1.98	1.99	1.98	2.00	1.99	1.97	2.01	2.00	2.00	2.00	2.02	1.99
Fe2+	2.17	2.18	2.24	2.30	2.20	2.18	2.28	2.25	2.20	2.13	2.17	2.18	2.26	2.31	2.31	2.27	2.16	2.20	2.28	2.28
Mn	0.45	0.45	0.43	0.21	0.19	0.19	0.28	0.34	0.40	0.45	0.43	0.41	0.29	0.27	0.22	0.19	0.16	0.18	0.19	0.22
Mg	0.31	0.27	0.24	0.34	0.49	0.51	0.36	0.26	0.20	0.15	0.16	0.18	0.29	0.35	0.42	0.47	0.57	0.54	0.47	0.40
Ca	0.10	0.10	0.10	0.17	0.14	0.15	0.11	0.20	0.25	0.30	0.27	0.25	0.17	0.11	0.09	0.09	0.15	0.11	0.11	0.11
tot. cat.	8.02	8.01	8.01	8.00	8.01	8.02	8.02	8.02	8.02	8.01	8.01	8.01	8.00	8.02	8.03	8.01	8.01	8.02	8.03	8.01
Alm	0.72	0.73	0.74	0.76	0.73	0.72	0.75	0.74	0.72	0.70	0.72	0.72	0.75	0.76	0.76	0.75	0.71	0.73	0.75	0.76
Gro	0.03	0.03	0.03	0.06	0.05	0.05	0.04	0.06	0.08	0.10	0.09	0.08	0.06	0.04	0.03	0.03	0.05	0.04	0.03	0.04
Prp	0.10	0.09	0.08	0.11	0.16	0.17	0.12	0.08	0.07	0.05	0.05	0.06	0.10	0.12	0.14	0.15	0.19	0.18	0.16	0.13
Sps	0.15	0.15	0.14	0.07	0.06	0.06	0.09	0.11	0.13	0.15	0.14	0.14	0.10	0.09	0.07	0.06	0.05	0.06	0.06	0.07
X_{Fe}	0.87	0.89	0.90	0.87	0.82	0.81	0.86	0.90	0.91	0.94	0.93	0.92	0.89	0.87	0.84	0.83	0.79	0.80	0.83	0.85

	CEEA-2-C4/Grt 2A reported on Fig. 13																			
Spots	Outer rim	Inner rim				Core												Inner rim		Outer rim
	1	2	3	4	6	8	10	11	13	18	22	25	27	30	31	32	33	34	35	37
SiO2	36.74	37.03	37.00	36.91	36.27	36.20	36.15	36.36	36.53	36.35	36.31	36.34	36.44	36.58	36.51	36.74	36.63	37.06	37.12	36.76
TiO2	0.06	0.06	0.04	0.07	0.04	0.00	0.03	0.07	0.05	0.04	0.03	0.08	0.02	0.00	0.02	0.00	0.04	0.04	0.01	0.00
Al2O3	20.99	21.09	21.06	20.85	20.72	20.90	20.70	20.71	20.57	20.63	20.65	20.66	20.65	20.98	21.23	21.14	21.16	21.54	21.25	21.33
FeO	33.88	33.61	32.96	32.68	35.01	35.27	34.58	33.96	33.56	32.24	33.20	34.66	34.58	35.08	34.83	34.03	32.78	32.71	32.55	32.92
MnO	2.56	1.47	1.26	1.67	2.50	2.69	3.10	3.63	4.07	4.66	4.17	3.61	3.20	2.61	2.63	2.44	2.39	2.40	2.46	3.27
MgO	3.31	4.35	4.83	4.75	2.37	2.14	1.95	1.71	1.50	1.29	1.42	1.72	1.90	2.40	3.05	3.63	4.30	4.53	4.69	4.03
CaO	2.06	2.06	1.95	2.16	2.23	2.04	2.47	2.91	3.22	3.79	3.31	2.67	2.61	2.14	1.38	1.26	1.23	1.31	1.23	1.61
Na2O	0.04	0.00	0.00	0.01	0.00	0.00	0.01	0.00	0.04	0.00	0.05	0.04	0.01	0.00	0.00	0.00	0.00	0.02	0.03	0.05
K2O	0.00	0.01	0.05	0.01	0.00	0.00	0.02	0.01	0.02	0.03	0.01	0.01	0.00	0.00	0.00	0.00	0.00	0.00	0.03	0.00
Cr2O3	0.07	0.07	0.03	0.09	0.02	0.00	0.03	0.01	0.03	0.02	0.01	0.01	0.01	0.01	0.00	0.01	0.00	0.00	0.01	0.00
Total	99.71	99.7	99.1	99.2	99.1	99.2	99.0	99.3	99.5	99.0	99.1	99.7	99.4	99.8	99.6	99.2	98.5	99.6	99.3	99.96
Si	2.97	2.97	2.98	2.97	2.97	2.96	2.97	2.98	2.99	2.99	2.98	2.97	2.98	2.97	2.96	2.98	2.97	2.97	2.98	2.96
Ti	0.00	0.00	0.00	0.00	0.00	0.00	0.00	0.00	0.00	0.00	0.00	0.00	0.00	0.00	0.00	0.00	0.00	0.00	0.00	0.00
Al	2.00	2.00	2.00	1.98	2.00	2.02	2.00	2.00	1.98	2.00	2.00	1.99	1.99	2.01	2.03	2.02	2.02	2.03	2.01	2.02
Fe2+	2.29	2.26	2.22	2.20	2.40	2.42	2.38	2.32	2.30	2.21	2.28	2.37	2.37	2.38	2.36	2.30	2.22	2.19	2.19	2.21
Mn	0.18	0.10	0.09	0.11	0.17	0.19	0.22	0.25	0.28	0.32	0.29	0.25	0.22	0.18	0.18	0.17	0.16	0.16	0.17	0.22
Mg	0.40	0.52	0.58	0.57	0.29	0.26	0.24	0.21	0.18	0.16	0.17	0.21	0.23	0.29	0.37	0.44	0.52	0.54	0.56	0.48
Ca	0.18	0.18	0.17	0.19	0.20	0.18	0.22	0.26	0.28	0.33	0.29	0.23	0.23	0.19	0.12	0.11	0.11	0.11	0.11	0.14
tot. cat.	8.02	8.03	8.02	8.03	8.03	8.03	8.03	8.02	8.02	8.01	8.02	8.03	8.02	8.02	8.02	8.01	8.01	8.01	8.01	8.03
Alm	0.753	0.73	0.72	0.71	0.78	0.79	0.77	0.76	0.75	0.73	0.75	0.77	0.77	0.78	0.77	0.76	0.73	0.72	0.72	0.724
Grs	0.059	0.05	0.05	0.06	0.06	0.05	0.07	0.08	0.09	0.11	0.09	0.07	0.07	0.06	0.04	0.03	0.03	0.03	0.03	0.045
Prp	0.131	0.17	0.19	0.18	0.09	0.08	0.07	0.06	0.06	0.05	0.05	0.06	0.07	0.09	0.12	0.14	0.17	0.18	0.18	0.158
Sps	0.058	0.03	0.02	0.03	0.05	0.06	0.07	0.08	0.09	0.10	0.09	0.08	0.07	0.05	0.06	0.05	0.05	0.05	0.05	0.073
XFe	0.85	0.81	0.79	0.79	0.89	0.90	0.91	0.92	0.93	0.93	0.93	0.92	0.91	0.89	0.86	0.84	0.81	0.80	0.80	0.82

	CEE3-3-C2/Grt 2B reported on Fig. 14																			
Spots	Outer rim	Inner rim		Outer core				Inner core					Outer core					Inner rim		Outer rim
	1	5	15	17	26	32	35	37	57	78	113	123	125	127	131	144	172	183	190	192
SiO2	37.18	37.30	37.77	37.72	37.34	37.06	37.38	37.50	37.74	37.58	37.87	37.29	37.25	36.85	37.36	37.40	37.06	37.66	38.25	37.97
TiO2	0.08	0.10	0.07	0.06	0.06	0.11	0.04	0.03	0.03	0.02	0.02	0.01	0.07	0.14	0.11	0.06	0.07	0.06	0.09	0.11
Al2O3	20.97	20.80	21.20	21.35	20.88	21.09	20.78	21.06	21.08	21.07	21.42	21.11	20.97	20.88	20.89	21.11	21.26	21.51	21.19	21.30
FeO	34.40	33.38	32.51	33.19	32.79	31.63	32.68	32.54	32.54	32.85	33.72	33.05	31.59	30.63	30.89	34.08	34.45	32.82	33.27	34.49
MnO	2.45	1.79	2.68	2.67	3.76	4.22	4.85	3.32	2.65	3.44	2.93	3.01	3.37	4.79	5.05	2.66	2.12	2.33	2.25	2.21
MgO	3.49	4.63	4.86	4.18	1.52	1.67	2.72	3.86	3.89	3.59	4.11	4.07	3.21	1.76	1.27	2.04	3.59	5.00	4.32	3.68
CaO	2.02	2.10	1.74	2.01	4.75	5.22	3.12	2.38	2.80	2.31	1.87	1.77	4.15	5.30	5.73	4.02	1.48	1.31	2.02	2.08

(*continued on next page*)

Table 6 (*continued*)

CEE3-3-C2/Grt 2B reported on Fig. 14

Spots	Outer rim	Inner rim		Outer core				Inner core					Outer core					Inner rim		Outer rim
	1	5	15	17	26	32	35	37	57	78	113	123	125	127	131	144	172	183	190	192
Na2O	0.02	0.03	0.00	0.01	0.00	0.00	0.01	0.03	0.01	0.00	0.00	0.01	0.01	0.01	0.01	0.00	0.00	0.02	0.02	0.00
K2O	0.00	0.00	0.00	0.00	0.00	0.03	0.00	0.00	0.03	0.00	0.01	0.00	0.00	0.00	0.01	0.02	0.01	0.00	0.00	0.00
Cr2O3	0.01	0.09	0.01	0.03	0.03	0.00	0.01	0.03	0.00	0.03	0.01	0.02	0.01	0.00	0.04	0.00	0.00	0.02	0.07	0.04
Total	100.6	100.2	100.8	101.2	101.1	101.0	101.6	100.7	100.8	100.9	102.0	100.3	100.6	100.4	101.4	101.4	100.0	100.7	101.5	101.9
Si	2.98	2.98	2.99	2.98	2.99	2.97	2.98	2.99	3.00	2.99	2.98	2.98	2.98	2.97	2.99	2.99	2.98	2.98	3.01	2.99
Ti	0.00	0.01	0.00	0.00	0.00	0.01	0.00	0.00	0.00	0.00	0.00	0.00	0.00	0.01	0.01	0.00	0.00	0.00	0.01	0.01
Al	1.98	1.96	1.98	1.99	1.97	1.99	1.95	1.98	1.97	1.98	1.99	1.99	1.98	1.98	1.97	1.99	2.01	2.01	1.96	1.98
Fe2+	2.31	2.23	2.15	2.20	2.20	2.12	2.18	2.17	2.16	2.19	2.22	2.21	2.11	2.07	2.07	2.28	2.32	2.17	2.19	2.27
Mn	0.17	0.12	0.18	0.18	0.26	0.29	0.33	0.22	0.18	0.23	0.20	0.20	0.23	0.33	0.34	0.18	0.14	0.16	0.15	0.15
Mg	0.42	0.55	0.57	0.49	0.18	0.20	0.32	0.46	0.46	0.43	0.48	0.48	0.38	0.21	0.15	0.24	0.43	0.59	0.51	0.43
Ca	0.17	0.18	0.15	0.17	0.41	0.45	0.27	0.20	0.24	0.20	0.16	0.15	0.35	0.46	0.49	0.34	0.13	0.11	0.17	0.18
tot. cat.	8.03	8.03	8.02	8.02	8.02	8.03	8.04	8.02	8.01	8.02	8.02	8.02	8.03	8.03	8.02	8.02	8.01	8.01	8.00	8.01
Alm	0.75	0.72	0.70	0.72	0.72	0.69	0.70	0.71	0.71	0.72	0.73	0.72	0.69	0.67	0.68	0.75	0.77	0.72	0.73	0.75
Gro	0.06	0.06	0.05	0.06	0.13	0.15	0.09	0.07	0.08	0.06	0.05	0.05	0.12	0.15	0.16	0.11	0.04	0.04	0.06	0.06
Prp	0.14	0.18	0.19	0.16	0.06	0.07	0.10	0.15	0.15	0.14	0.16	0.16	0.12	0.07	0.05	0.08	0.14	0.19	0.17	0.14
Sps	0.05	0.04	0.06	0.06	0.08	0.09	0.11	0.07	0.06	0.08	0.06	0.07	0.07	0.11	0.11	0.06	0.05	0.05	0.05	0.05
XFe	0.85	0.80	0.79	0.82	0.92	0.91	0.87	0.83	0.82	0.84	0.82	0.82	0.85	0.91	0.93	0.90	0.84	0.79	0.81	0.84

CEE3-3-C3/Grt 2B reported on Fig. 15

Spots	Outer rim	Inner rim			Outer Core			Inner core				Outre core			Inner rim			Outer rim
	2	5	7	13	15	22	35	39	45	53	57	66	73	80	87	93	99	101
SiO2	37.14	37.02	37.20	37.49	37.60	37.10	37.82	37.40	37.43	37.31	37.59	37.10	37.29	37.66	37.88	37.38	37.01	37.05
TiO2	0.16	0.13	0.04	0.03	0.03	0.06	0.03	0.02	0.16	0.05	0.03	0.05	0.04	0.01	0.02	0.18	0.10	0.07
Al2O3	20.62	20.61	21.24	21.08	20.95	21.21	21.30	21.20	21.02	20.83	21.01	21.06	20.88	21.42	21.59	21.01	21.10	20.73
FeO	34.47	33.20	33.16	32.46	33.83	34.52	34.22	33.53	32.83	31.82	33.80	33.72	33.88	34.39	33.46	33.62	33.55	34.74
MnO	3.22	3.17	2.88	2.34	1.89	2.27	3.24	3.42	3.42	4.86	3.30	4.19	3.14	2.46	2.28	1.97	1.98	3.04
MgO	2.36	4.14	4.58	4.87	4.61	3.88	3.06	2.92	3.19	3.26	2.89	2.47	3.24	4.01	4.69	4.28	3.97	2.70
CaO	2.05	1.73	1.26	1.69	1.32	1.23	2.22	2.40	2.71	2.50	2.46	2.69	2.06	1.28	1.22	2.15	2.14	2.01
Na2O	0.03	0.01	0.03	0.01	0.03	0.01	0.00	0.06	0.00	0.03	0.00	0.01	0.03	0.01	0.05	0.01	0.00	0.00
K2O	0.01	0.02	0.00	0.04	0.02	0.00	0.00	0.00	0.02	0.00	0.01	0.00	0.00	0.01	0.01	0.02	0.00	0.04
Cr2O3	0.08	0.03	0.02	0.02	0.01	0.03	0.01	0.02	0.01	0.00	0.01	0.02	0.02	0.02	0.01	0.02	0.04	0.08
Total	100.1	100.1	100.4	100.0	100.3	100.3	101.9	101.0	100.8	100.6	101.1	101.3	100.6	101.3	101.2	100.6	99.9	100.4
Si	3.01	2.98	2.97	2.99	3.00	2.97	2.99	2.99	2.99	2.99	3.00	2.97	2.99	2.99	2.99	2.98	2.97	2.99
Ti	0.01	0.01	0.00	0.00	0.00	0.00	0.00	0.00	0.01	0.00	0.00	0.00	0.00	0.00	0.00	0.01	0.01	0.00
Al	1.97	1.96	2.00	1.98	1.97	2.00	1.99	2.00	1.98	1.97	1.98	1.99	1.97	2.00	2.01	1.97	2.00	1.97
Fe2+	2.33	2.23	2.21	2.16	2.26	2.31	2.26	2.24	2.19	2.13	2.26	2.26	2.27	2.28	2.21	2.24	2.25	2.35
Mn	0.22	0.22	0.19	0.16	0.13	0.15	0.22	0.23	0.23	0.33	0.22	0.28	0.21	0.17	0.15	0.13	0.13	0.21
Mg	0.28	0.50	0.54	0.58	0.55	0.46	0.36	0.35	0.38	0.39	0.34	0.30	0.39	0.47	0.55	0.51	0.48	0.32
Ca	0.18	0.15	0.11	0.14	0.11	0.11	0.19	0.21	0.23	0.21	0.21	0.23	0.18	0.11	0.10	0.18	0.18	0.17
tot. cat.	8.00	8.04	8.03	8.02	8.01	8.02	8.01	8.01	8.01	8.02	8.01	8.03	8.02	8.01	8.01	8.03	8.02	8.02
Alm	0.77	0.72	0.72	0.71	0.74	0.76	0.75	0.74	0.72	0.70	0.74	0.74	0.75	0.75	0.73	0.73	0.74	0.77
Gro	0.06	0.05	0.04	0.05	0.04	0.03	0.06	0.07	0.08	0.07	0.07	0.08	0.06	0.04	0.03	0.06	0.06	0.06
Prp	0.09	0.16	0.18	0.19	0.18	0.15	0.12	0.12	0.13	0.13	0.11	0.10	0.13	0.16	0.18	0.17	0.16	0.11
Sps	0.07	0.07	0.06	0.05	0.04	0.05	0.07	0.08	0.08	0.11	0.07	0.09	0.07	0.05	0.05	0.04	0.04	0.07
XFe	0.89	0.82	0.80	0.79	0.80	0.83	0.86	0.87	0.85	0.85	0.87	0.88	0.85	0.83	0.80	0.81	0.83	0.88

link with the melting processes and show different chemical characters compared to Grt2A. It probably belongs to a previous metamorphic event and is therefore probably of xenolithic origin.

7.1. Interpretation of garnets textures and chemistry

Garnet is a common accessory mineral in granite, which provides important information about the petrogenesis of its host granite. Compositional zoning of garnet can be used to constrain the nature, the physicochemical conditions, and the processes of granitic magma evolution (Lackey et al., 2006, 2011; Dahlquist et al., 2007; Erdmann et al., 2009; Villaros et al., 2009a,b; Harris and Vogeli, 2011; Scallion et al., 2011).

Garnet composition and zoning depend on the global chemical composition of the system and *PT* conditions. So the bell shaped spessartine zoning profile highlights the prograde garnet growth during a single metamorphic or anatectic event (e.g. Hollister, 1966; Dahlquist et al., 2007). This is due to the ability of garnet to incorporate Mn more easily than do other phases, which generates a Rayleigh fractionation process while Mn gets exhausted in the matrix. Pyrope shows a reverse zoning, incorporating more and more Mg during temperature increase, whereas almandine and grossular have various zoning profiles depending on continuous and discontinuous reactions. On the other hand, the variation of the X_{Fe} ratio is similar to the variation of the spessartine during the prograde growth of garnet and can also give specific information on *PT* conditions (e.g Hauzenberger et al., 2005).

Complex garnet zoning is generally associated with polyphased metamorphic (or melting) events. Compared to simple zoning profiles of garnets developed during a single metamorphic event, complex ones are more difficult to analyse and interpret, both for prograde and retrograde metamorphic conditions, but they potentially provide more information on the PT paths.

Textural patterns of Grt1 in the CEE (see 4.2 and 6.1 sections) are similar to those described by Álvarez-Valero and Kriegsman (2007) in

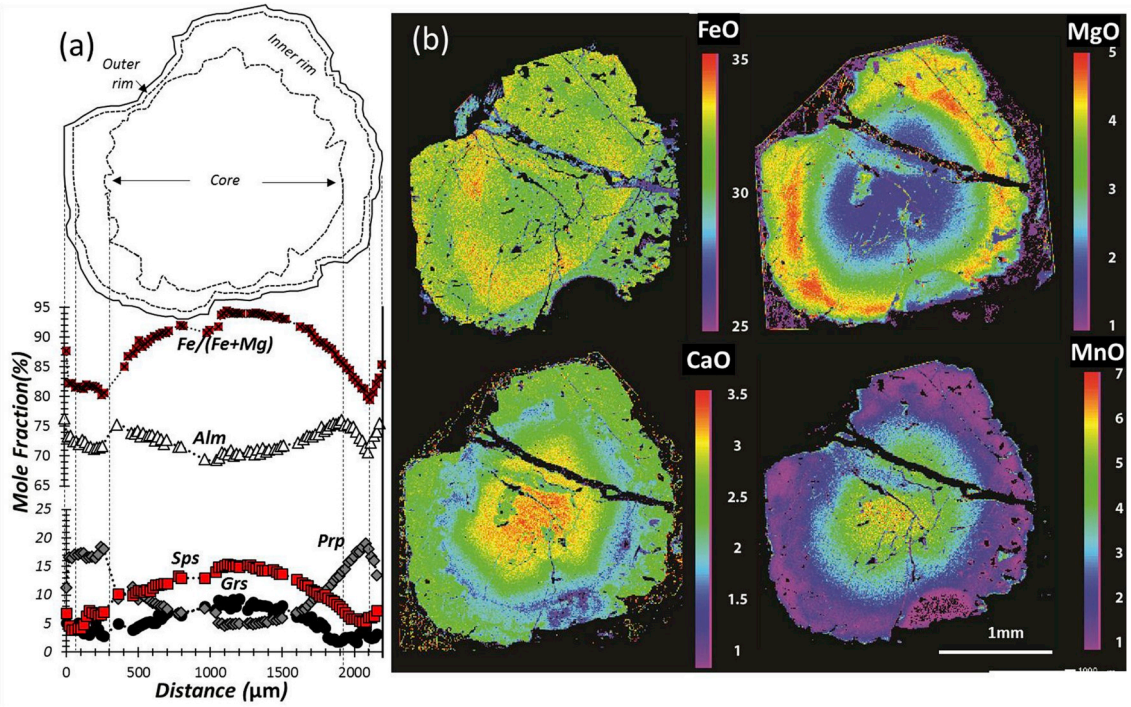

Fig. 12. a and b: Zoning profiles and chemical maps of CEE's Grt2A. (Sample CEE3-3-C1, Table 6).

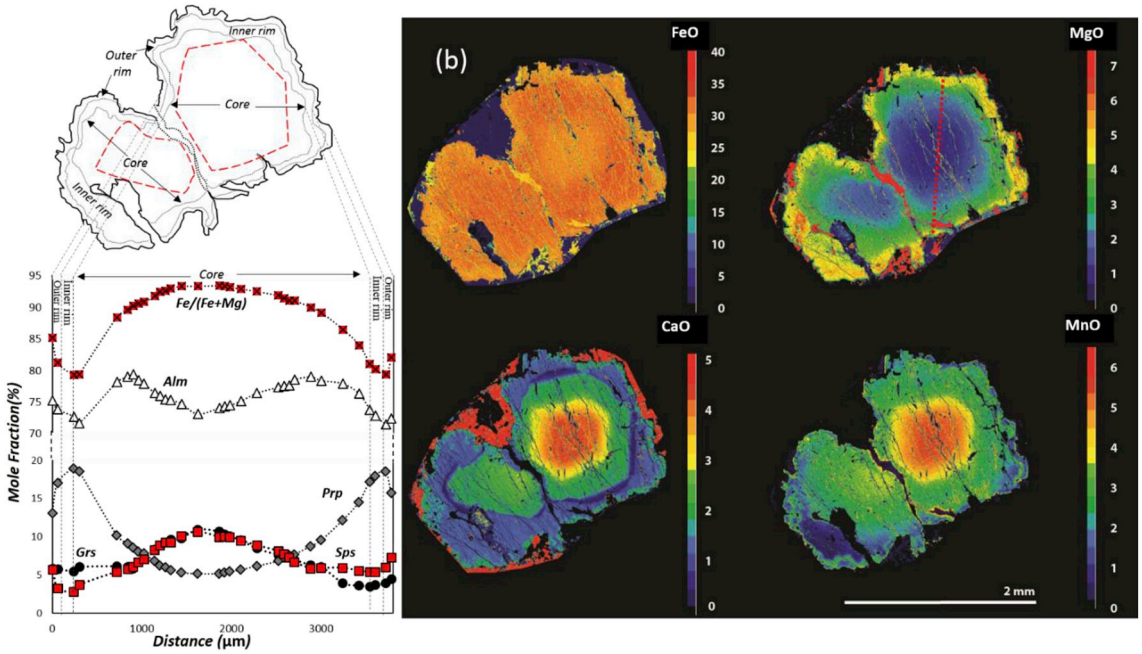

Fig. 13. a and b: Zoning profiles and chemical maps of two amalgamated garnets 2A grains in CEE garnetites (Sample CEEA-2-C4, Table 6).

metasedimentary xenoliths embedded within dacites of the Neogene Volcanic Province (NVP) of SE Spain. Their homogeneous chemistry does not provide much information on their genesis.

Grt2A crystals in the CEE display zoning patterns (see section 5.6) that record early, prograde growth in the core domains, followed by partial resorption in the rim areas where the zoning was reversed. These latter features indicate dissolution and reprecipitation of garnet at its contact with crystallising melt forming the granitic matrix or groundmass (Yu and Lee, 2016). The preservation of centimetre-scale zoning patterns of all end-members suggests that the residence time of the crystals under high-T conditions was relatively short (Caddick et al., 2010).

The zoning patterns of Grt2B crystals in the CEE (see section 5.6) record a more complex history than Grt2A. Flat inner core patterns indicate a high residence time under high-T conditions during or after their growth. The Grt2B outer core and rims patterns exhibiting the bell shaped profiles for Sps, Grs and X_{Fe} and reverse bell-shaped profile for Prp (Table 8) are similar to those of Grt2A cores and rims. They indicate their development under the same chemical and physical conditions as mentioned in the paragraph above. Furthermore, the independent core zoning and the common rim zoning of amalgamated Grt2 grains (section 4.6, Fig. 8d–e, 9e and 13b) indicate that the rims of theses garnets were formed after their amalgamation. It suggests that they have been separately transported from their source, were then deposited in the

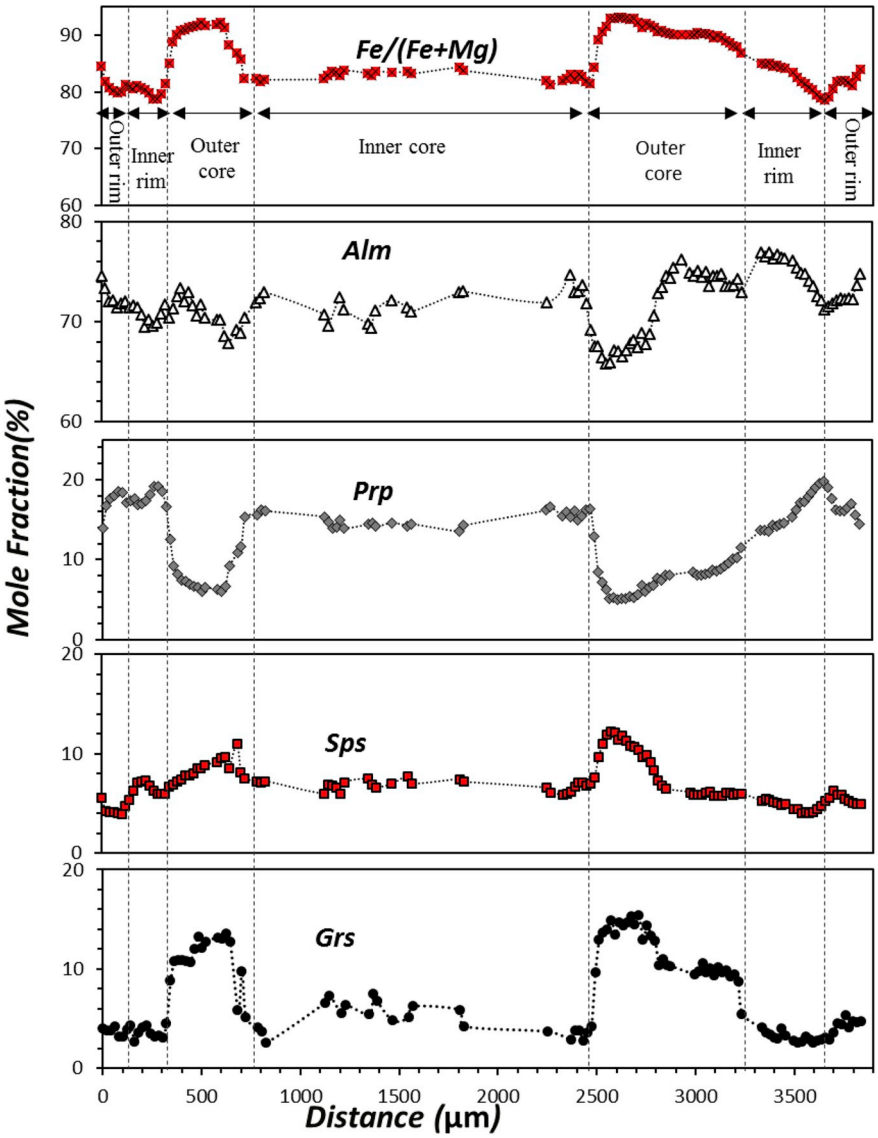

Fig. 14. Typical end-member zoning profiles of CEE's Grt2B (Sample CEE3-3-C2, Table 6).

CEE xenolith-cumulate deposit, and were subsequently welded together before the final melt crystallised and reacted with them.

7.2. Origin and signification of Aouli Mibladen garnets

Garnet 1: The reaction forming the original mineral association, Grt1 enclosing Bt, Sill and Qtz cannot be established. This association is surrounded by a Crd1 + Spl + Pl + Ilm corona. This textural pattern underlines a reaction between Grt1 and matrix during the anatectic event producing the Crd + Spl + Ilm + Pl corona (Álvarez-Valero et al., 2000, 2007 and Álvarez-Valero and Waters, 2010). The corona separates Grt1 from the granitic groundmass. Grt1 has therefore grown during a metamorphic event that took place prior to the partial melting processes.

Garnet 2. Garnets 2A and 2B have many characteristics of peritectic, transported and accumulated garnets. Peritectic origin of Grt2 is supported by: i) its presence in anatexites as a product of biotite incongruent dehydration melting reactions of metapelitic rocks; ii) the analogy of the garnet concentration patterns with those described in many peraluminous granites where peritectic origin, transport and amalgamation of garnets are well documented (Cesare et al., 1997; Dorais et al., 2009, 2012 Villaros et al., 2009a,b; Stevens et al., 2007; Taylor and Stevens, 2010); iii) bell-shaped zoning profiles for Mn, Ca, Mg and X_{Fe} exhibiting by Grt2A attesting to their formation during one prograde stage of metamorphism/melting. In Grt2 the inclusion-free rims, with different chemical characteristics compared to their cores, were likely formed after amalgamation of transported garnets as a result of dissolution/resorption and reprecipitation phenomena at the contact with crystallizing peraluminous granitic melts. The transport and accumulation of peritectic garnets is evidenced by their occurrences in the granitic groundmass as veins or pockets of rounded and euhedral millimetric to centimetric grains. These latters are often broken and dislocated, indicating that they were subjected to magma transport and flow. In addition, some of these fragments are enclosed by minerals that define the granitic groundmass. Fragments of Grt2A have been recognized in evolved peraluminous granites of the Perdreaux and Poulet stocks.

Grt2B has the same characters as Grt2A except for its inner core that corresponds to an earlier metamorphic garnet onto which the peritectic garnet, similar to Grt2A, has grown. As mentionned above, internal cores of Grt2B have many characteristics comparable to those of Grt1.

7.3. Evolution of anatectic melts

The produced peraluminous granitic melts had probably evolved from the less peraluminous Crd-bearing anatectic granites to more

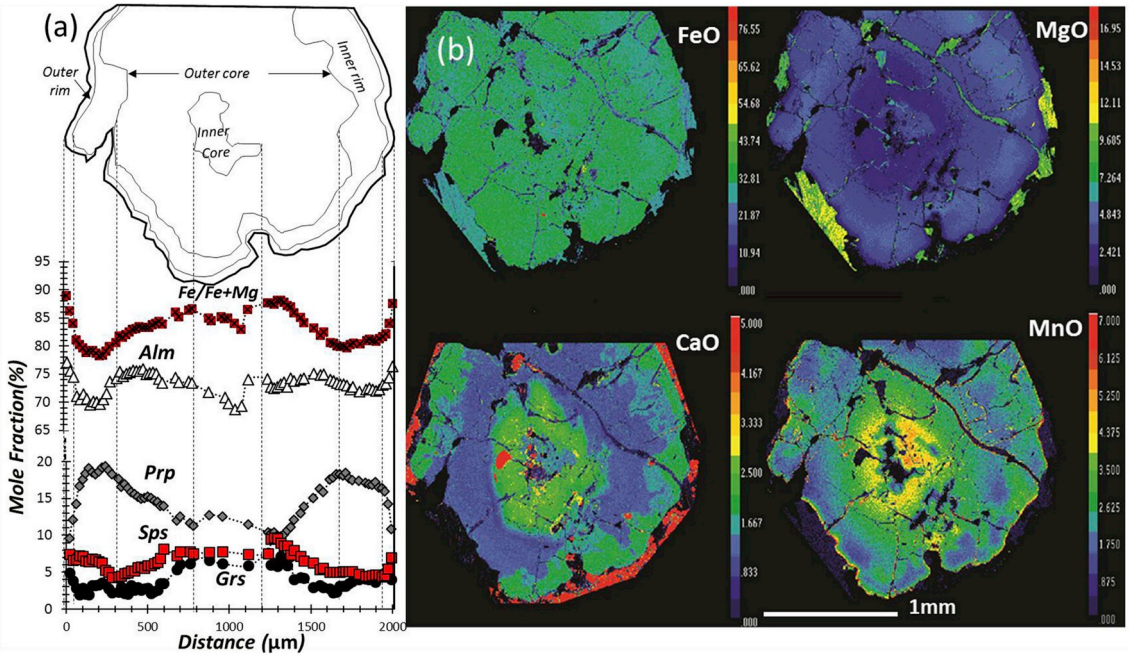

Fig. 15. a) Zoning profile of CEE's garnet 2B using chemical end-member fractions. b) Chemical maps of garnet 2B grains in CEE garnetite (Sample CEE3-3-C3, Table 6).

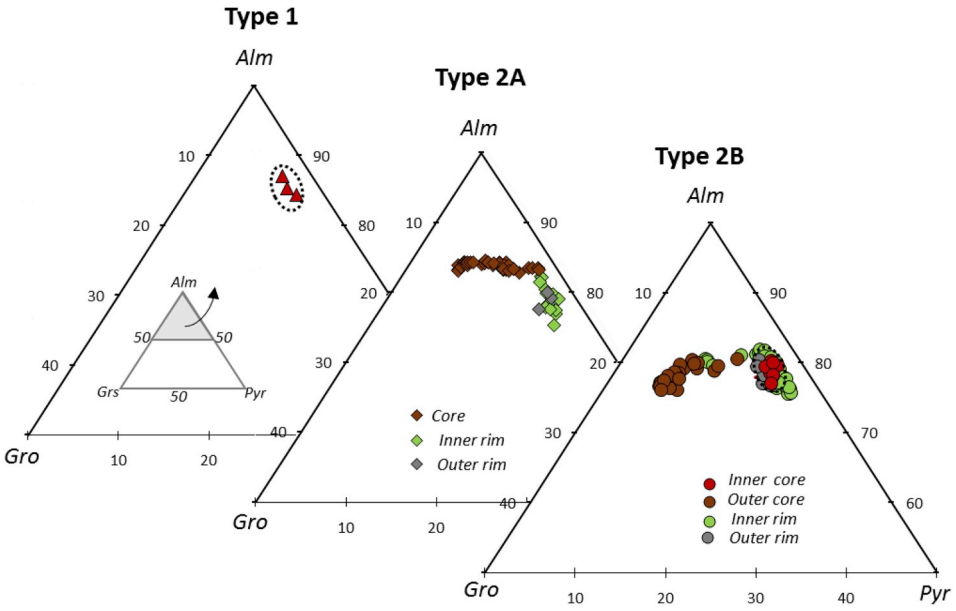

Fig. 16. Comparison between CEE's Grt1, Grt2A and Grt2B compositions in terms of almandine, grossular and pyrope end-members.

peraluminous ones that are Crd-bearing microgranitic dykes and then two-mica granites of the Perdreaux and Poulet stocks (see Fig. 3a, see also Tartèse and Boulvais, 2010). These latter evolved granites show, indeed, many features, like the presence of sillimanite, cordierite and garnet crystals that suggests probable genetic links between the whole of S-types rocks.

8. Thermodynamic modelling and P-T conditions of anatexis

Here we applied thermodynamic modelling in order to estimate the thermodynamic conditions of the partial melting process. The calculation of a pseudosection aims at retrieving pressure and temperature at fixed composition, hence, the crucial question when is to choose the right whole rock composition of the protolith that has undergone metamorphic and melting processes. We consider, for our themodynamic calculations, a large sample of HLA layered migmatite (sample migt2, Table 1) including mesosome (40%) melanosome (30%) +leucosome (30%) considered to be a good representatives of the paleosome instead of neosome including leucosome and melanosome (sample mgt1, Table 1). Paleosome is, following Kriegsman (2001a), representative of the original metapelite protolith.

Thermodynamic modelling is done in the system $MnO–TiO_2–Na_2O–CaO–K_2O–FeO–MgO–Al_2O_3–SiO_2–H_2O$ (MnTiNCKFMASH) using the thermodynamic data file named hp02ver.dat (see www.perplex.ethz.ch/, updated on January 2017). The pseudosection is contructed for *P-T* conditions varying between 600 and 1000 °C and 2–8 kbar. The end-members and corresponding solid solutions used are given in Table 9. They correspond to the most consistent internally

Table 7
Summary of petrographic and chemical characteristics of the four Crd types in Aouli-Mibladen anatexites and their petrogenetic significance.

Occurrences	CEE	CEE and HLA anatectic granites	CEE and HLA anatectic granites	CEE
Shape	Conotic	Anhedral	Euhedral	Coronitic
Cordierite types	Crd1	Crd2	Crd3	Crd4
Photomicrographs	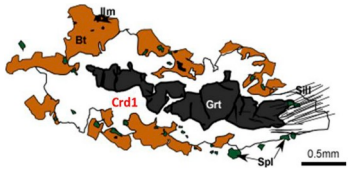	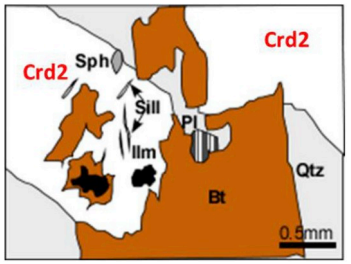	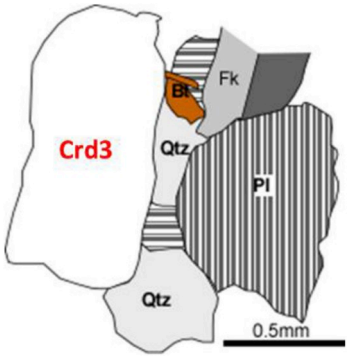	
Chemical characters	MgO = 7.2%–7.85% FeO = 9.2%–9.7% X_{Fe} = 0.4 to 0.43	MgO = 4.7%–7.6% FeO = 9.3%–10.7% X_{Fe} = 0.37	MgO = 1.4%–4.7% FeO = 4.2%–13.8% X_{Fe} = 0.6	MgO = 4.68% FeO = 10.68% X_{Fe} = 0.56
inclusions	Spl, Ilm, Bt	Bt, Sill, Ilm	Free	Bt
Nature, origin and/ or PT evolution	Prograde, developed during partial melting processes (Álvarez-Valero et al., 2007)	Prograde, peritectic; product of Bt dehydration melting reactions (Thompson, 1982; Carrington and Harley, 1995; Spear et al., 1999)	Cotectic, crystallised from anatectic melts (Barbey et al., 1999)	Retromorphic (Yardley, 1989; Aranovich and Podlesski, 1983)

Table 8
Summary textural and chemical variabilities of garnets in Aouli-Mibladen anatexites and their petrogenetic significance.

	Garnet 1	Garnet 2A		
Occurrences	CEE	CEE and HLA anatectic granites		
Shape	Anhedral	Euhedral		
Chemical zoning	No	**Core** Mn, Ca and XFe Bell shaped profiles. Mg Reverse bell-shaped profile	**Inner rim** no	**Outer rim** no
Chemical characters	Sps = 14.5% Prp = 9% XFe = 88%	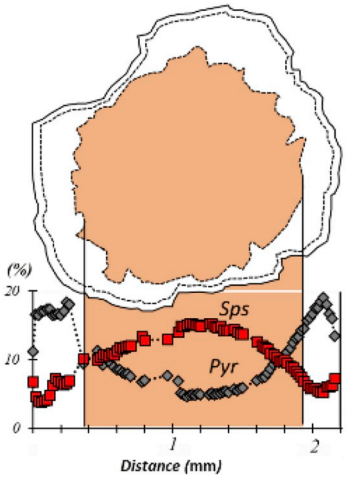 Sps = 5.3%–15% Prp = 4.6% 18.8% XFe = 79%–93.5%	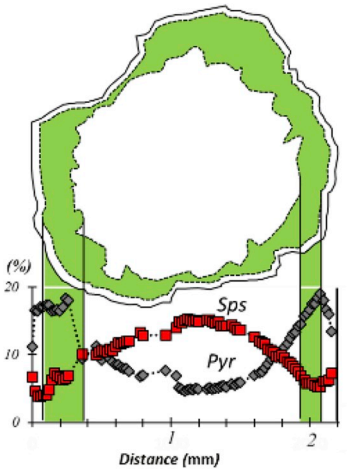 Sps = 2.8%–6% Prp = 16%–18.5% XFe = 80%–82%	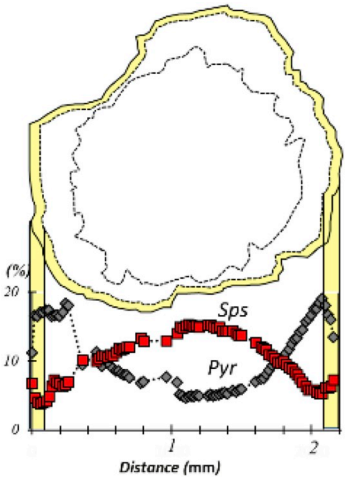 Sps = 7.4% Prp = 13% XFe = 83%–87%
inclusions	Bt, Sill, Qtz	Bt, Pl, Qtz	Free	Free
Nature, origin and/or PT evolution	Metamorphic, xenolithic (Álvarez-Valero et al., 2007)	Prograde, Peritectic; product of pelites partial melting processes	Retromorphic. Dissolution followed by reprecipitation during melt crystallization	Subsolidus reequilibration
		Cesare et al. (1997); Dorais et al. (2009), 2012 Villaros et *al.*, 2009; Stevens et al. (2007); Taylor and Stevens (2010); Yu and Lee (2016)		

(*continued on next page*)

Table 8 (*continued*)

	Garnet 2B			
Occurrences	CEE and HLA anatectic granites			
Shape	Euhedral			
Chemical zoning	**Inner core** No	**Outer core** Mn, Ca and XFe Bell shaped profiles. Mg reverse bell-shaped profile	**Inner rim** No	**Outer rim** No
Chemical characters	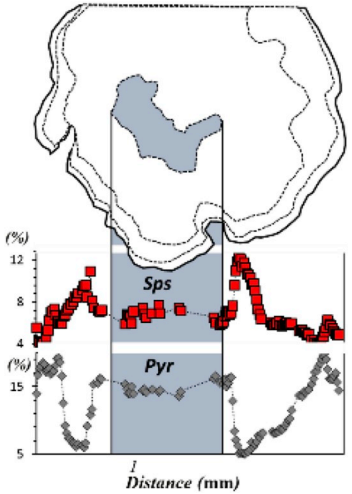 Sps = 7% Prp = 14% XFe = 83%–87%	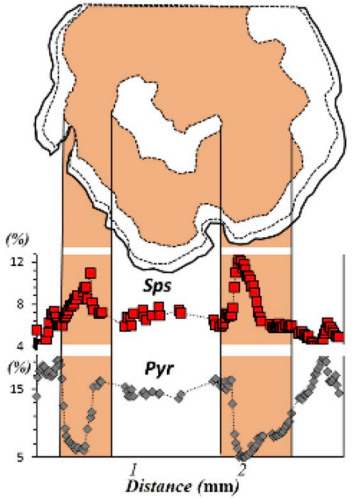 Sps = 5%–12% Prp = 5%–17% XFe = 80%–93%	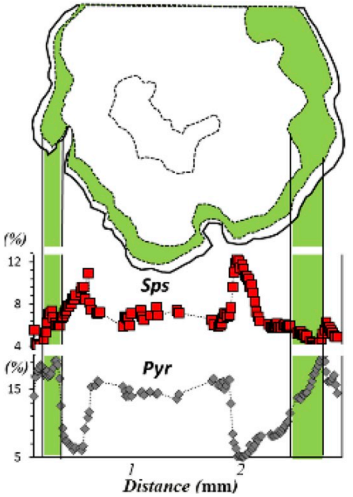 Sps = 4%–7% Prp = 15%–18.5% XFe = 81%	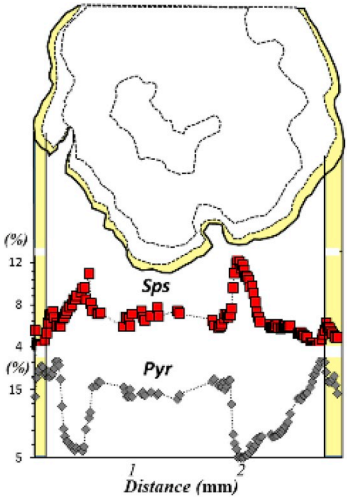 Sps = 5%–7.3% Prp = 11%–17% XFe = 82%–88%
inclusions	Bt,Sill, Qtz	Bt, Pl, Qtz	Free	Free
Nature, origin and/ or PT evolution	Metamorphic (xenolithic)	Prograde, Peritectic; product of pelites partial melting processes	Retromorphic. Dissolution followed by reprecipitation during melt crystallization	Subsolidus reequilibration

Cesare et al. (1997); Dorais et al. (2009), 2012 Villaros et *al.*, 2009; Stevens et al. (2007); Taylor and Stevens (2010); Yu and Lee (2016)

Table 9
Phase end-members used for the pseudosection calculations.

Mineral	Solid solution model	Endmembers
Plagioclase	Pl (I1,HP)	an, ab, abh,
K-feldspar	Kf	kspL, mic, abh, san
Biotite	Bio(TCC)	mfbit, ffbit, fbit, mtbit, ftbit, tbit, mts, sdph, east, mnbi, ann, phl
Mica	Mica (CHA)	naph, mu, pa, cel, fcel, ma
Chlorite	Chl (HP)	daph, ames, afchl, clin
Orthopyroxene	Opx (HP)	en, fs
Garnet	Gt (HP)	spss, alm, py, gr
Staurolite	St (HP)	mnst, fst, mst
Cordierite	hCrd	fcrd, crd, hcrd
Ilmenite	Ilm (WPH)	png, geik, hem, oilm, dilm
Melt	melt (HP)	heoL, fo8L, fa8L,abL, sil8L, anL, kspL, Q8l

dataset named solution_model.dat in Perple_X package (see www.perplex.ethz.ch/, updated on August 2017). H_2O contents used for *P-T* calculations are assumed to be equal to the LOI values obtained during analyses procedures (H_2O^+).

The calculated pseudosection is presented in Fig. 17a. For the chosen rock composition the grid shows multivariant mineral associations dominated by tri-, quadri- and penta-variant fields. Divariant fields are scarce, and fields with $V > 6$ are mostly restricted at the high temperature side of the pseudosection. The solidus curve corresponds to the H_2O saturated pelite solidus reaction (Kf + Pl + Qtz + Bt + Mus + H_2O = Melt, after Thompson, 1982), and the Bt-out curve may correspond to the biotite dehydration melting reactions producing a larger volume of granitic melts (Spear et al., 1999). Cordierite is restricted to pressures lower than 6.3 kbar (blue area in Fig. 17b). Garnet is present at a pressure greater than 3.5 kbar for melt-bearing assemblages (pink area, Fig. 17b). Grt + Crd + melt-bearing assemblages are restricted to the purple area (Fig. 17b) for a temperature greater than 700 °C and a pressure varying from 3 to 6.3 kbar, whereas garnet bearing assemblages beyond the Bt-out curve are stable at pressures greater than 6.3 kbar.

The observed mineral association in migmatites, anatectic granites and the CEE granitic groundmass containing garnet and cordierite as peritectic phases, are stable over a large *P-T* domain varying from 3.2 to 6.3 kbar in a temperature range varying from 800 to 850 °C corresponding to the beginning of biotite dehydration melting reactions (fields 17 and 23 in Fig. 17a) to more than 900 °C corresponding to large melt fractions in high-variance fields ($V > 6$) beyond the biotite out curve (fields 24 in Fig. 17a).

Perple_X modelling using the Werami routine of coexisting mineral compositions, mainly cordierite, garnet and biotite (both restitic and cotectic) leads to a more precise *P-T* vector corresponding to their growth (Fig. 17b). The vector is drawn from the intersection of primary metamorphic Bt1 and Grt2A inner core X_{Fe} isopleths at 630–650 °C (star 1). These PT conditions correspond to fields 35 and 37 of the pseudosection in Fig. 17a below the wet solidus of granites where garnet 2A starts growing under metamorphic conditions at the beginning of the rapid and important temperature increase. Then the PT vector reaches star 2 corresponding to the intersection of peritectic Crd X_{Fe} and the external parts of Grt2A core X_{Mn} and X_{Fe} isopleths at 850 °C (star 2). This vector corresponds to an isobaric heating.

On the other hand, petrographical and mineralogical study have shown that Grt2 underwent two growth steps. The prograde growth is followed by resorption/dissolution and reprecipitation stage leading to a retrograde growth of garnet rims. Garnet rims have grown in equilibrium with cotectic Bt2 crystallising from granitic melt. Isopleth intersection of garnet rims and cotectic biotite X_{Fe}, indicate 680 °C and 3.2 kbar (star 3) as *P-T* conditions of this equilibrium (Fig. 17b). These conditions are in accordance with the X_{Fe} isopleth of Crd4 aureoles surrounding Grt2 that intersect biotite and garnet rims isopleths at the same conditions of star 3 (i.e. 680 °C and 3.2 kbar, Fig. 17b).

9. Discussion and petrogenetic model

The definition of a petrologic model for Aouli-Mibladen S-type granitic rocks must integrate data provided in this work. These data are related to petrographic and chemical characters of anatectic rock types and minerals as well as their relationships with associated M-I type rock series. According to Dahire (2004) these latter comprise two main magmatic sequences. The first one that regroups the most mafic calc-alkaline rocks (gabbro-diorites and granodiorites), was originated from partial melting of lithospheric mantle wedge (M-type) and differenciated by AFC (Assimilation Fractional Crystallization) processes. The second comprises the calc-alkaline suite of monzogranites, grey and pink granites resulting from melting of igneous photoliths (I-type) in the lower crust and from the interaction (mixing) with mantle-derived magmas and their fractionated melts at different crustal levels. These M-I type rock series are closely associated with S-type suite whose study in this work brings more information allowing a better knowledge of the petrogenetic evolution of the whole of this granitic complex.

S-type rock series occur as: i) anatexites, including migmatites and anatectic granites of HLA and CEE; ii) Crd-bearing microgranitic dykes and; iii) two mica granites. Anatexites correspond to partially (migmatite) and/or entirely (granite) melted metapelites in HLA area. Anatectic melts underwent fractional crystallization processes with successively anatectic granites of HLA and CEE, Crd-bearing microgranitic dykes and two mica-granites. Several arguments are in agreement with fractional crystallization of Bt + Pl + Kf ± Crd3 assemblages from anatectic melts: i) lower amounts of Bt in microgranitic dykes then in two-micas leucogranites; ii) high SiO2 contents from HLA anatectic granites to Perdreaux and Poulet leucogranites (Table 1); iii) increasing of peraluminous character in the same way (Fig. 3a). These genetic links are also supported by the presence of cotectic Crd3 in leucogranites dykes and the occurrence of garnet fragments in Poulet leucogranites. In addition, Perdreaux and Poulet two-mica leucogranitic stocks develop their own contact metamorphism area which overprints the metamorphic aureole of the Aouli-Mibladen complex.

Mingling and limited mixing features between metaluminous grey granites and HLA peraluminous anatectic granites indicate their concomitant final emplacement. Such features are common in granitic complexes, partially melted metapelitic rocks having served as melt-lubricated zones facilitating the ascent of the whole of the complex (Clemens and Mawer, 1992). The CEE is a small stock of anatectic granites containing metasedimentary xenoliths and garnets as cumulates. Its internal structures show that this configuration is due to the transportation and accumulation of these solid phases by anatectic melts. Density contrasts between these solid phases and the anatectic melt, as well as the viscosity of this latter are responsible of selective entrainment (Taylor and Stevens, 2010) and final amalgamation into the CEE structural trap during magma ascent.

The crystallization of peraluminous anatectic melts led to coarse-grained anatexites characterized by an overall mineral association Bt + Pl + Kf + Qtz ± Crd ± Grt + Ilm. Nevertheless key minerals such as Bt, Crd and Grt having various textural and chemical characteristics belong to specific mineral associations. These characteristics combined with thermodynamic constraints allow to define several stages for the continuous evolution of this anatectic suite: i) stage 1 corresponds to a metapelitic protholith equilibrated at 6 kbar and 600 °C containing Grt1 grains that belongs to a previous metamorphic event; ii) stage 2 includes anatexites where Crd2 and Grt2 are the main peritectic phases produced by Bt1 dehydration melting processes at 6 kbar and 850 °C. The development of Crd1 corona around Grt1 is associated with this stage; iii) stage 3 characterized by the formation of cotectic Crd 3 and Crd 4 coronas around Grt2 as well as Bt2 linked to the crystallization and emplacement of produced anatectic melt during a general retrogression at 3 kbar and 700 °C.

These petrological observations as well as the thermodynamic modelling constrain the metamorphic and magmatic evolution of this part of the Moroccan Variscan belt. Relationships between M-I type magmatic suite (from gabbros to pink granites) and the S-type suite

show the direct mantle-crust interaction during an orogenic episode. Fig. 18 illustrates the following petrogenetic model for the Aouli-Mibladen granitic complex. In the left side of the figure are specified the, known or supposed, natures and ages of protoliths and their metamorphic facies at different levels of reconstituted Variscan crust. To the right side, along the grey arrow, are mentioned the successive main

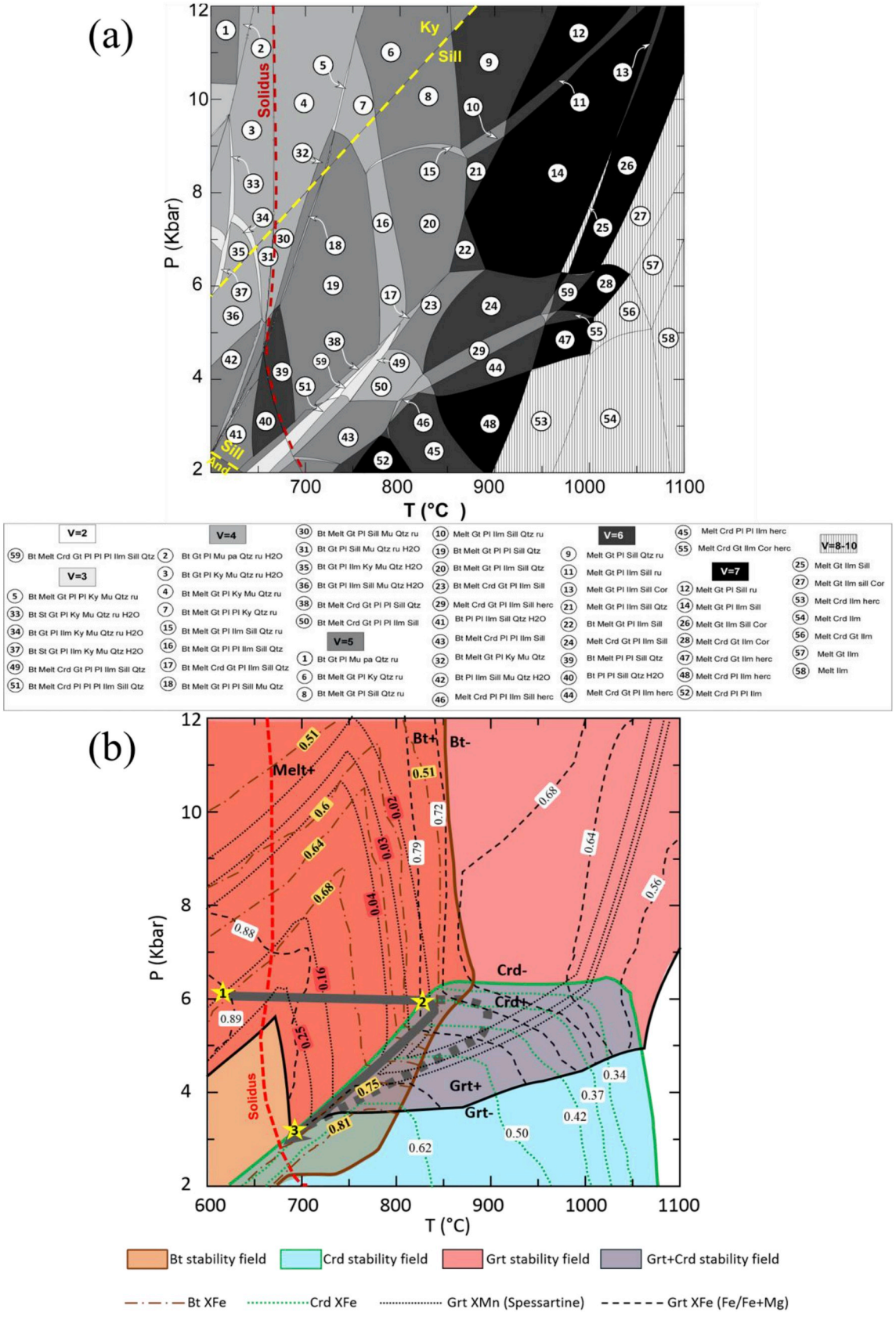

(caption on next page)

Fig. 17. a) P-T pseudosection calculated for the HLA migmatites sample "MIGT2" composition (Table 1) using Perple_X software (Connolly, 2005, 2009; Connolly and Petrini, 2002). Solid solution models used are reported in Table 9. Heavy dotted red line represents the H2O-saturated pelite solidus. b) Simplified P-T pseudosection after Fig. 17a using the Werami routine of the Perple_X software, showing the stability fields of the major phases as well as their compositional isopleths in molar fractions. Star 1 = PT conditions defined by the intersection between Grt2A core center isopleths for X_{Mn} and X_{Fe} and Bt1 X_{Fe} isopleth; Star 2 = PT conditions for the mineral associations in garnet and cordierite bearing anatectic granites defined by the intersection between Grt2A core margins isopleths for X_{Mn} and X_{Fe} and Crd2 X_{Fe} isopleth. Star 3- PT conditions corresponding to the intersection between Grt2A internal rim isopleths for X_{Mn}, for Bt2 X_{Fe} isopleth and for Crd4 X_{Fe} isopleth.

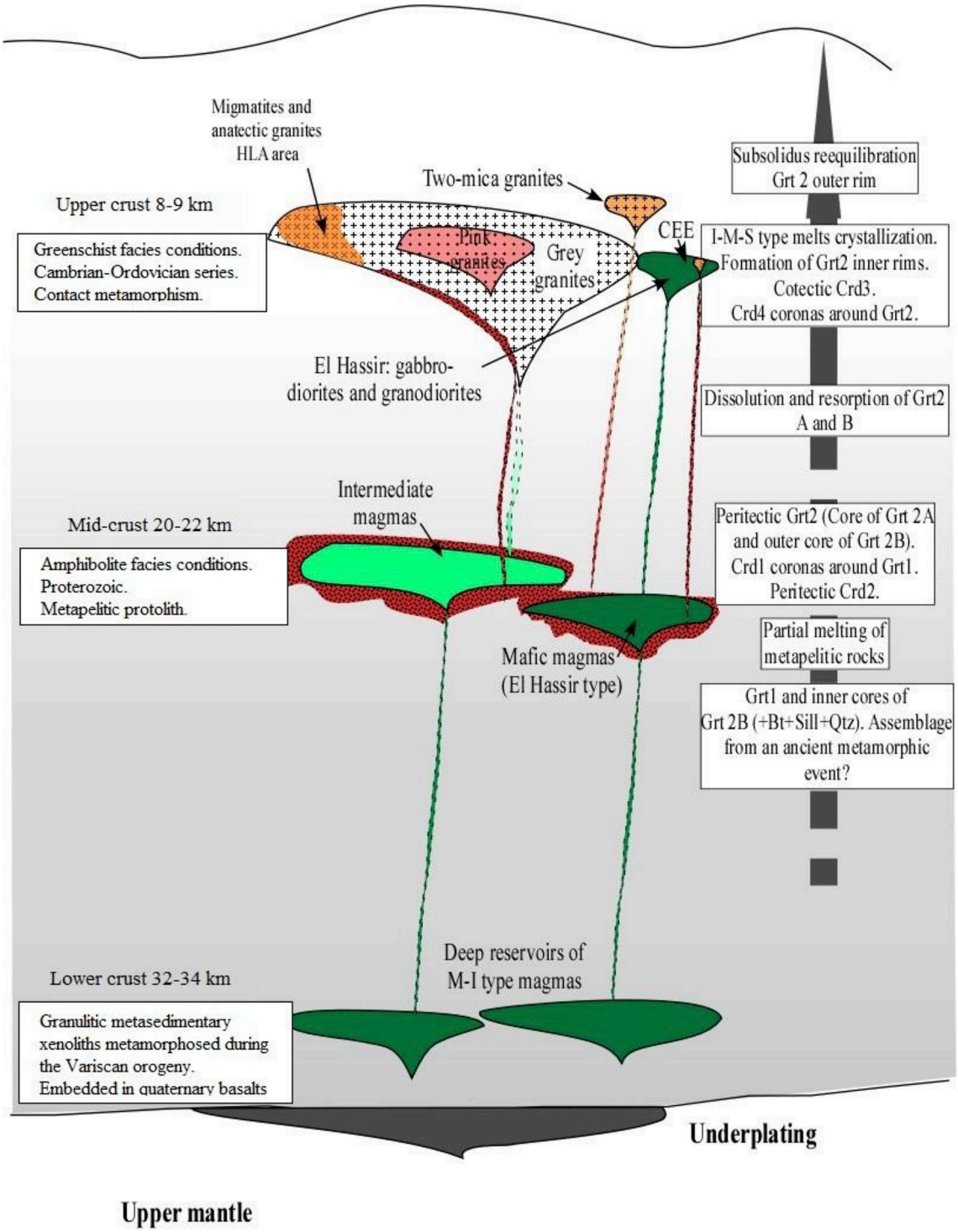

Fig. 18. Petrogenetic model proposed for the evolution of the Aouli-Mibladen complex during the Variscan orogeny (see text for explanations, not on scale).

steps of Aouli-Mibladen S-type series petrogenetic evolution during the Variscan orogeny, with special emphasis to Grt and Crd minerals. In the middle of the figure are represented the different components and stages of the complex evolution. Thereby during the Variscan orogeny, lithospheric mantle and igneous infracrustal protholiths underwent partial melting processes leading to mafic magmas underplating and storage in the lower crust levels. Their emplacement in large reservoirs at nearly 20 km depth leads an isobaric heating and consequently the melting of the surrounding metamorphic metapelitic protolith. Melting is located around the M-I-type magmas immediate surrounding and do not form migmatitic and anatectic complexes as in the Western Europe Variscan domain. Later differentiated M-I-type and S-type sets are emplaced concomitantly with limited mixing and mingling during their final crystallization at a depth of 8–9 km estimated from the PT conditions of the contact metamorphism aureole (600 °C, 3 kbar).

10. Regional implications

Direct data on the petrogenetic processes in the lower and middle crust and their thermal state during the Variscan orogeny in Moroccan Mesetas still scarce or are missing. Data from the lower crust are derived from Moukadiri (1999) and Hoeflaken (2012) who have studied the metasedimentary xenoliths embedded within quaternary alkali basalts in the Alpine Middle-Atlas belt. They define the peak metamorphic PT conditions (10 kbar and 900–950 °C) corresponding to UHT metamorphism operated during the Variscan orogeny at approximatively 300 Ma (Monazite age; Hoeflaken, 2012). Informations on the middle crust are based on geochemical and geochronological indirect studies in the Western Meseta part of the Moroccan Variscan belt. Among others, Essaifi et al. (2014) recent studies in Jebilet massif, shows that mantle-derived magmas underwent mixing processes leading to the formation of the observed bimodal association of mafic and granitic rocks while the associated peraluminous leucogranites are of pure sedimentary crustal origin whose protolith is of Proterozoic age based on its TDM (1.76–0.85 Ga). The emplacement ages of the bimodal association and leucogranites are respectively 330 Ma and 300 Ma. The existence of Proterozoic terranes is now well documented in the Western Meseta. U—Pb zircon ages were obtained directly on granitic rocks of Goida (625–600 Ma, Ouabid et al., 2017) or on rhyolitic porphyry in Rehamna massif (2.05 Ga, Pereira et al., 2015). Indirect U—Pb zircon dating determined on inherited zircons in Tiflet granites provides ages of 609 to 605 Ma (Tahiri et al., 2010) while zircon crystals contained in mid-crustal felsic granulite xenoliths embedded in Triassic lamprophyres in Jebilet massif provide ages of 280–328 Ma; 540–615 Ma, 700 Ma and 2Ga (Dostal et al., 2005). These results confirm the existence of a Proterozoic basement below the Palaeozoic formations in the Western Meseta.

In the Aouli-Mibladen granitic complex, belonging to the eastern Moroccan Variscan Meseta, petrogenetic processes operating in the middle crust, lacking in the Western Meseta, are well illustrated. They exhibit the nature of the interaction, during the Variscan orogeny, between mantle-derived magmas and Proterozoic protholith at 20–22 km depth before their final emplacement in shallower levels. These processes, must be confirmed by new dating campaign, could therefore be generalized to the whole of Moroccan Variscan domain and integrated in the multidisciplinary geotectonic models (Roddaz et al., 2002; Hoepfner et al., 2006; Michard et al., 2008, 2010).

Acknowledgments

We thank very much Prof. Omar Saddiqi and Prof. Michele Zucali for their constructive reviews that greatly improved the quality of this paper. This work benefited from the financial and technical support of LGRN (Laboratoire de Géodynamique et Ressources Naturelles) of Dhar El Mahraz Faculty of Sciences. Fez University. Morocco; and CNRS-GET (Centre National de la Recherche Scientifique and Géosciences Environnement Toulouse, France).

Appendix A. Supplementary data

Supplementary data to this article can be found online at https://doi.org/10.1016/j.jafrearsci.2019.03.006.

References

Abaché, I., Kimba, I., 2011. Pétrologie des xénolithes métasedimentaires du complexe granitique d'Aouli-Mibladen (Meseta Orientale, Maroc). MSc thesis. Géologie. Université sidi Mohammed ben Abdellah, Faculté des sciences Dhar Mahrez 132 pp.
Álvarez-Valero, A.M., Kriegsman, L.M., 2007. Crustal thinning and mafic underplating beneath the Neogene Volcanic Province (Betic Cordillera, SE Spain): evidence from crustal xenoliths. Terra. Nova 19, 266–271.
Álvarez-Valero, A.M., Waters, D.J., 2010. Partially melted xenoliths as a window into sub-volcanic processes: evidence from the Neogene magmatic province of the Betic Cordillera, SE Spain. J. Petrol. 51 (5), 973–991.
Álvarez-Valero, A.M., Cesare, B., Kriegsman, L.M., 2007. Formation of melt-bearing spinel– cordierite–feldspars coronas after garnet in metapelitic xenoliths. Reaction modelling and geodynamic implications. J. Metamorph. Geol. 25, 305–320.
Aranovich, L.Y., Podlesskii, K.K., 1983. The cordierite-garnet-sillimanite-quartz equilibrium: experiments and applications. In: In: Saxena, S.K. (Ed.), Kinetics and Equilibrium in Mineral Reactions. Advances in Physical Geochemistry, vol. 3 Springer, New York, NY.
Asrat, A., Barbey, P., Ludden, J.N., Reisberg, L., Gleizes, G., Ayalew, D., 2004. Petrology and isotope geochemistry of the pan-african Negash pluton, northern Ethiopia: mafic–felsic magma interactions during the construction of shallow-level calc-alkaline plutons. J. Petrol. 45, 1147–1179.
Barbarin, B., 1990. Granitoids: main petrogenetic classifications in relation to origin and tectonic setting. Geol. J. 25, 227–238.
Barbey, P., Macaudière, J., Nzenti, J.P., 1990. High-pressure dehydration melting of metapelites: evidence form the migmatites of Yaoundé (Cameroon). J. Petrol. 31, 401–427.
Barbey, P., Marignac, J.M., Montel, J.M., Macaudière, J., Gasquet, D., Jabbori, J., 1999. Cordierite growth textures and the conditions of genesis and emplacement of crustal granite magmas: the Velay Granite complex (Massif Central, France). J. Petrol. 40, 1425–1441.
Baxter, S., Feely, M., 2002. Magma mixing and mingling textures in granitoids: examples from the Galway Granite, Connemara, Ireland. Mineral. Petrol. 76, 63–74.
Bouloton, J., 1992. Mise en évidence de cordiérite héritée des terrains traversés dans le pluton granitique de Oulad Ouaslam (Jebilet, Maroc). Can. J. Earth Sci. 29, 658–668.
Bouloton, J., El Amrani, I., El Mouraouah, A., Montel, J.M., 1991. Les xénolithes peralumineux des granites, d'après l'exemple du pluton superficiel des Oulad Ouaslam (Jebilet, Maroc). Comptes Rendus de l'Académie des Sciences, série 11 (312), 273–279.
Boushaba, A., 1984. Contribution à la connaissance géologique du complexe granitique du Ment et de son encaissant (Maroc central). Étude pétrologique, géochimique et structurale. Thèse de 3ème cycle. Univ. Mohammed V 186 pp.
Brown, M., Solar, G.S., 1999. The mechanism of ascent and emplacement of granite magma during transpression: a syntectonic granite paradigm. Tectonophysics 312, 1–33.
Caddick, M.J., Konopásek, J., Thompson, A.B., 2010. Preservation of garnet growth zoning and the duration of prograde metamorphism. J. Petrol. 51, 2327–2347.
Carignan, J., Hild, P., Mevelle, G., Morel, J., Yeghicheyan, D., 2001. Routine Analyses of Trace Elements in Geological Samples Using Flow Injection and Low Pressure On-Line Liquid Chromatography Coupled to ICP-MS: A Study of Geochemical Reference Materials BR, DR-N, UB-N, AN-G and GH, vol. 25. Geostandards Newsletter, pp. 187–198.
Carrington, D.P., Harley, S.L., 1995. Partial melting and phase relations in high-grade metapelites: an experimental petrogenetic grid in the KFMASH system. Contrib. Mineral. Petrol. 120, 270–291.
Cesare, B., Savioli Mariani, E., Venturelli, G., 1997. Crustal anatexis and melt extraction during deformation in the restitic xenoliths at El Joyazo (SE Spain). Mineral. Mag. 61, 15–27.
Chappell, B.W., 1999. Aluminum saturation in I- and S-type granites and the characterization of fractionated haplogranites. Lithos 46, 535–551.
Chappell, B.W., White, A.J.R., 1974. Two contrasting granite types. Pac. Geol. 8, 173–174.
Chappell, B.W., White, A.J.R., 2001. Two contrasting granite types, 25 years later. Aust. J. Earth Sci. 48, 489–499.
Chemseddoha, A., 1986. Cisaillement ductile et granite syntectonique dans les Jebilets Centrales: l'exemple du pluton hercynien d'Oulad Ouslam (Massif des Jebilets), Meseta Sud marocaine. Thèse de 3ème cycle. Rennes 155 pp.
Clauer, N., Jeannette, D., Tisserant, D., 1980. Datations isotopiques des cristallisations successives d'un socle hercynien et cristallophyllien (Haute Moulouya, Moyen Maroc). Geol. Rundsch. 69, 63–83.
Clemens, J.D., Mawer, C.K., 1992. Granitic magma transport by fracture propagation. Tectonophysics 204, 339–360.
Connolly, J.A.D., Petrini, K., 2002. An automated strategy for calculation of phase diagram sections and retrieval of rock properties as a function of physical conditions. Journal of Metamorphic Petrology 20, 697–708.
Connolly, J.A.D., 2005. Computation of phase equilibria by linear programming: a tool for geodynamic modelling and its application to subduction zone decarbonation. Earth Planet. Sci. Lett. 236, 524–541.
Connolly, J.A.D., 2009. The geodynamic equation of state: what and how. Geochem.

Geophys. Geosyst. 10, Q10014. https://doi.org/10.1029/2009GC002540.
Dahire, M., Ribeiro, M.L., Ntarmouchant, A., El Boukhari, A., Pons, J., Driouch, Y., Ben Abbou, M., Moreira, E., 2002. Les granitoïdes hercyniens : cas du complexe de la Haute Moulouya (Meseta orientale, Maroc) et ses associations shoshonitique à peralumineuse. Commun. Inst. Geol. e Mineiro 89, 249–264.
Dahire, M., 2004. Le complexe plutonique de la Haute Moulouya (Meseta oriental, Maroc) : Evolution pétrologique et structurale. Unpublished PhD thesis. Mohamed Ben Abdellah University, Fès (Morocco) 322 pp.
Dahlquist, J.A., Galindo, C., Pankhurst, R.J., Rapela, C.W., Alasino, P.H., 2007. Magmatic evolution of the Peñón Rosado granite: petrogenesis of garnet-bearing granitoids. Lithos 95, 177–207.
Dahmani, M., Sawyer, E.W., 2001. Variabilité géochimique des métapélites dans l'auréole métamorphique d'Oulmès (Maroc central). Bulletin de l'Institut Scientifique, section Sciences de la Terre 23, 7–20.
Diot, H., Bouchez, J.L., 1989. Les ghranitoïdes hercyniens de la Haute Moulouya (Maroc) : leur structure primaire déduite de l'ASM. Indications sur leur mise en place. Bull. Soc. Géol 705–716 France, (8), t. V.
Dostal, J., Keppie, J.D., Hamilton, M.A., Aarab, E.M., Lefort, J.P., Murphy, J.B., 2005. Crustal xenoliths in Triassic lamprophyre dykes in western Morocco: tectonic implications for Rheic Ocean suture. Geol. Mag. 142, 159–172.
Dorais, M.J., Pett, T.K., Tubrett, M., 2009. Garnetites of the Cardigan Pluton, New Hampshire: evidence for peritectic garnet and implications for source rock compositions. J. Petrol. 50, 1993–2016.
Dorais, M.J., Tubrett, M., 2012. Detecting peritectic garnet in the peraluminous Cardigan pluton, New Hampshire. J. Petrol. 53, 299–324.
El Hadi, H., Tahiri, A., Reddad, A., 2003. Les granitoïdes hercyniens post-collisionnels du Maroc oriental: une province magmatique calco-alcaline à shoshonitique. C. R. Géosciences 335, 959–967.
El Mourouah, A.E.A., 1993. Genèse et mise en place des granitoïdes. Cas de la Haute Moulouya (Meseta Orientale, Maroc). Implications géodynamiques. Thèse ès Sci. Marrakech, 288 pp.
Emberger, A., 1965. Introduction à l'étude des minéralisations plombifères de la Haute Moulouya. Notes et mém. Serv. Géol., Maroc 181 197-174.
Erdmann, S., Jameson, R.A., Macdonald, M.A., 2009. Evaluating the origin of garnet, cordierite, and biotite in granitic rock: a case study from the South Mountain Batholith, Nova Scotia. J. Petrol. 50, 1477–1503.
Essaifi, A., Samson, S., Goodenough, K., 2014. Geochemical and Sr–Nd isotopic constraints on the petrogenesis and geodynamic significance of the Jebilet magmatism (Variscan Belt, Morocco). Geol. Mag. 151, 666–691.
Filali, F., Guiraud, M., Burg, J.-P., 1999. Nouvelles données pétro-structurales sur la boutonnière d'Aouli (Haute Moulouya) : leurs conséquences sur la géodynamique hercynienne au Maroc. Bull. Soc. Geol. France 4, 435–450.
Filali, F., 1996. Etude pétro-structurale de l'encaissant métamorphique de la boutonnière d'Aouli-Mibladen (Haute Moulouya, Maroc) : conséquences sur la géodynamique hercynienne au Maroc. Thèse du Muséum National d'Histoire Naturelle, Paris 193 pp.
Gasquet, D., Bouloton, J., 1995. Les filons de microdiorites des Jbilet Centrales (Meseta marocaine): pré-rifting permien ? In: Réunion Extraordinaire SGF, Marrakech (Maroc), pp. 55 (abstract).
Gasquet, D., Stussi, J.M., Nachit, H., 1996. Les granitoïdes hercyniens du Maroc dans le cadre de l'évolution géodynamique régionale. Bull. Soc. Geol. France 167/4, 517–528.
Gasquet, D., 1991. Genèse d'un pluton composite tardi-hercynien. Le massif de Tichka, Haut Atlas Occidental (Maroc). Thèse es-Sciences. Univ. Nancy 413 pp.
Ghaffari, M., Rashidnejad-Omran, N., 2014. Magma mixing/mingling in Salmas granodiorite, NW Iran: evidence from mafic microgranular enclaves. Arabian Journal of Geosciences 8, 7141–7152.
Guidotti, C.V., 1984. Micas in metamorphic rocks. In: In: Bailey, S.W. (Ed.), Micas, vol. 13. Mineralogical Society of America, Washington, D.C., pp. 357–467 Reviews in Mineralogy.
Haïmeur, J., Chabane, A., El Amrani, I.E., 2003. Analyse petrominéralogique des interactions granite-enclaves dans le pluton hercynien de Zaër (Maroc central) : implications pétrogénétiques. Bull. Inst. Sci. sect. Sci. Terre 25, 1–29.
Harris, C., Vogeli, J., 2011. Oxygen isotope composition of garnet in the Peninsula granite, Cape Granite Suite, South Africa: constraints on melting and emplacement mechanisms. S. Afr. J. Geol. 113, 401–412.
Hauzenberger, C.A., Robl, J., Stüwe, K., 2005. Garnet zoning in high pressure granulite-facies metapelites, Mozambique belt, SE-Kenya: constraints on the cooling history. Eur. J. Mineral. 17, 43–55.
Hoeflaken, J. van, 2012. Hercynian UHT Metamorphism of Crustal Xenoliths from Bou Ibalghatene and Tafraoute, Middle Atlas, Morocco. MSc thesis. Utrecht University, Netherlands 220 pp.
Hoepffner, C., Houari, M.R., Bouabdelli, M., 2006. Tectonics of the north african variscides (Morocco, western Algeria), an outline. In: In: Frizon de Lamotte, D., Saddiqi, O., Michard, A. (Eds.), Recent Developments on the Maghreb Geodynamics: C. R. Acad. Sci. Paris, Geoscience, vol. 338. pp. 25–40.
Hoepffner, C., 1982. Le magmatisme "pré et post-orogénique" hercynien dans le Paléozoïque des Rehamna. In: In: Michard, A. (Ed.), Le Massif des Rehamna (Maroc). Notes et Mém. Serv. Géol. Maroc, vol. 303. pp. 150–163.
Holland, T.J.B., Powell, R., 1998. An internally consistent thermodynamic data set for phases of petrological interest. J. Metamorph. Geol. 16, 309–343.
Hollister, L.S., 1966. Garnet zoning: an interpretation based on the Rayleigh fractionation model. Science 154, 1647–1651.
Kretz, R., 1983. Symbols for rock-forming minerals. Am. Mineral. 68, 277–279.
Kriegsman, L.M., Álvarez-Valero, A.M., 2010. Melt-producing versus melt-consuming reactions in pelitic xenoliths and migmatites. Lithos 116 (3–4), 310–320 May 2010.
Lackey, J.S., Erdmann, S., Hark, J.S., Nowak, R.M., Murray, K.E., Clarke, D.B., Valley, J.W., 2011. Tracing garnet origins in granitoid rocks by oxygen isotope analysis: examples from the South Mountain batholith, Nova Scotia. Can. Mineral. 49, 417–739.
Lackey, J.S., Valley, J.W., Hinke, H.J., 2006. Deciphering the source and contamination history of peraluminous magmas using $\delta^{18}O$ of accessory minerals: examples from garnet-bearing plutons of the Sierra Nevada batholiths. Contrib. Mineral. Petrol. 151, 20–44.
Mahmood, A., 1980. Étude pétrologique du granite hercynien de Zaër (Massif central marocain). Thèse d'Etat. Univ. Clermont Ferrand 421 pp.
Maniar, P.D., Piccoli, P.M., 1989. Tectonic discrimination of granitoids. Geol. Soc. Am. Bull. 101, 635–643.
Mengel, K., Richter, M., Johannes, W., 2001. Leucosome–forming small-scale geochemical processes in the metapelitic migmatites of the Turku area, Finland. Lithos 56, 47–73.
Michard, A., Hoepffner, C., Soulaimani, A., Baidder, L., 2008. The variscan belt. In: Michard, A., Saddiqi, O., Chalouan, A., Frizon de Lamotte, D. (Eds.), Continental Evolution: the Geology of Morocco. Springer, pp. 65–131.
Michard, A., Soulaimani, A., Hoepffner, C., Ouanaimi, H., Baidder, L., Rjimati, E.C., Saddiqi, O., 2010. the South-western branch of the variscan belt: evidence from Morocco. Tectonophysics 492, 1–24.
Milord, I., Sawyer, E.W., Brown, M., 2001. Formation of diatexite migmatite and granite magma during anatexis of semi pelitic metasedimentary rocks: an example from St. Malo, France. J. Petrol. 42, 487–505.
Montel, J.M., Marignac, C., Barbey, P., Pichavant, M., 1992. Thermobarometry and granite genesis: the Hercynian low-P, high-T Velay anatectic dome (French Massif Central). J. Metamorph. Geol. 10, 1–15.
Moukadiri, A., 1999. Essai de caractérisation de la lithosphère sous le Moyen Atlas (Maroc) par l'étude des xénolites mantelliques dans les basaltes alcalins. Thèse es sciences. Université Cadi Ayad, Marrakech 312 pp.
Moukadiri, A., Bouloton, J., 1998. Pétrologie des granulites exhumées par le volcanisme récent du Moyen Atlas, aperçu sur la croûte inférieure néogène du Maroc Central. C. R. Acad. Sci. Paris. Série 2a 327, 731–734.
Mrini, Z., Rafi, A., Duthou, J.L., Vidal, P., 1992. Chronologie Rb/Sr des granitoïdes hercyniens du Maroc, conséquences. Bull. Soc. Geol. Fr. 3, 281–291.
Nyman, M.W., Pattison, D.R.M., Ghent, E.D., 1995. Melt extraction during formation of K-feldspar sillimanite migmatites, west of Revelstoke, British Columbia. J. Petrol. 36, 351–372.
Ouabid, M., Ouali, H., Garrido, C.J., Acosta-Vigil, A., Roma´n-Alpiste, M.J., Dautria, J.M., Marchesi, C., Hidas, K., 2017. Neoproterozoic granitoids in the basement of the Moroccan central meseta: Correlation with the anti-atlas at the NW paleo-margin of gondwana. Precambrian Res. 299, 34–57.
Oukemeni, D., Bourne, J.H., 1994. Etude géochimique des granitoïdes du pluton d'Aouli, Haute Moulouya, Maroc. J. Afr. Earth Sci. 17/4, 429–433.
Oukemeni, D., 1993. Géochimie, géochronologie (U-Pb) du pluton d'Aouli et comparaisons géochimiques avec d'autres granitoïdes hercyniens du Maroc par analyse discriminante. Thèse Université Québec. Montréal 129 pp.
Pereira, M.F., El Houicha, M., Chichorro, M., Armstrong, R., Jouhari, A., El Attari, A., Ennih, N., Silva, J.B., 2015. Evidence of a Paleoproterozoic basement in the Moroccan Variscan Belt (Rehamna Massif, Western Meseta). Precambrian Res. 268, 61–73.
Roddaz, M., Brusset, S., Soula, J.-C., Debat, P., Ben Abbou, M., Beziat, D., Driouch, Y., Christophoul, F., Ntarmouchant, A., Deramond, J., 2002. Foreland basin magmatism in the Western Moroccan Meseta and geodynamic inferences. Tectonics 21 (5), 1043–1065.
Rose, F., 1987. Les types granitiques du Maroc hercynien. These doctorat. Universittf Paris VI, France 381pp.
Scallion, K.L., Jamieson, R.A., Barr, S.M., White, C.E., Erdmann, S., 2011. Texture and composition of garnet as a guide to contamination of granitoid plutons: an example from the governor lake area, Meguma terrane, Nova Scotia. Can. Mineral. 49, 441–458.
Spear, F.S., Kohn, M.J., Cheney, J.T., 1999. P–T paths from anatectic pelites. Contrib. Mineral. Petrol. 134, 17–32.
Stevens, G., Villaros, A., Moyen, J.F., 2007. Selective peritectic garnet entrainment as the origin of geochemical diversity in S-type granites. Geology 35, 9–12.
Tahiri, A., Montero, P., El Hadi, H., Martínez Poyatos, D., Azor, A., Bea, F., Simancas, F., González Lodeiro, F., 2010. Geochronological data on the Rabat–Tiflet granitoids:their bearing on the tectonics of the Moroccan Variscides. J. Afr. Earth Sci. 57, 1–13.
Tartèse, R., Boulvais, P., 2010. Differentiation of peraluminous leucogranites "en route" to the surface. Lithos 114, 353–368.
Tisserant, D., 1977. Les isotopes du Strontium et l'histoire hercynienne du Maroc. Etude de quelques massifs atlasiques et mésétiens. Thèse 3ème cycle, Strasbourg, 103pp.
Taylor, J., Stevens, G., 2010. Selective entrainment of peritectic garnet into S-type granitic magmas: evidence from Archaean mid-crustal anatectites. Lithos 120, 277–292.
Termier, H., Termier, G., 1971. Le massif granito-dioritique du Tichka (Haut Atlas Occidental, Maroc). In: Volume 1 : Les régions et les terrains Notes et Mémoires Service géologique Maroc, vol. 216 240 pp.
Thompson, A.B., 1982. Dehydration melting of pelitic rocks and the generation of H2O-undersaturated granitic liquids. Am. J. Sci. 282, 1567–1595.
Vanderhaeghe, O., Burg, J.-P., Teyssier, C., 1999. Exhumation of Migmatites in Two Collapsed Orogens: Canadian Cordillera and French Variscides, vol. 154. Geological Society Special Publications, pp. 181–204.
Villaros, A., Stevens, G., Moyen, J.F., Buick, I.S., 2009a. Tracking S-type granite from source to emplacement: clues from garnet in the Cape Granite Suite. Lithos 112, 217–235.

Villaros, A., Stevens, G., Moyen, J.F., Buick, I.S., 2009b. The trace element compositions of Stype granties: evidence for disequilibrium melting and accessory phase entrainment in the source. Contrib. Mineral. Petrol. 158, 543–561.
Wernert, P., Schulmann, K., Chopin, F., ŠtÍpská, P., Bosch, D., Elhouicha, M., 2016. Tectonometamorphic evolution of an intracontinental orogeny inferred from P−T−t−d paths of the metapelites from the Rehamna massif (Morocco). J. Metamorph. Geol. 34/9, 917–940.
White, A.J.R., Chappell, B.W., 1983. Granitoid Types and Their Distribution in the Lachlan Fold Belt, Southeastern Australia, vol. 159. Geological Society of America Memoirs, pp. 21–34.
White, A.J.R., Chappell, B.W., 1977. Ultrametamorphism and granitoid genesis. Tectonophysics 43, 7–22.
Yardley, B.W.D., 1989. An Introduction to Metamorphic Petrology. Longman Earth Sci. 1043 Series 248pp.
Yu, X., Lee, C.T.A., 2016. Critical porosity of melt segregation during crustal melting: constraints from zonation of peritectic garnets in a dacite volcano. Earth Planet. Sci. Lett. 449, 127–134.